

# Under-Oil Autonomously Regulated Oxygen Microenvironments: A Goldilocks Principle-Based Approach for Microscale Cell Culture

Chao Li,\* Mouhita Humayun, Glenn M. Walker, Keon Young Park, Bryce Connors, Jun Feng, Molly C. Pellitteri Hahn, Cameron O. Scarlett, Jiayi Li, Yanbo Feng, Ryan L. Clark, Hunter Hefti, Jonathan Schrope, Ophelia S. Venturelli,\* and David J. Beebe\*


Oxygen levels in vivo are autonomously regulated by a supply–demand balance, which can be altered in disease states. However, the oxygen levels of in vitro cell culture systems, particularly microscale cell culture, are typically dominated by either supply or demand. Further, the oxygen microenvironment in these systems is rarely monitored or reported. Here, a method to establish and dynamically monitor autonomously regulated oxygen microenvironments (AROM) using an oil overlay in an open microscale cell culture system is presented. Using this method, the oxygen microenvironment is dynamically regulated via the supply–demand balance of the system. Numerical simulation and experimental validation of oxygen transport within multi-liquid-phase, microscale culture systems involving a variety of cell types, including mammalian, fungal, and bacterial cells are presented. Finally, AROM is applied to establish a coculture between cells with disparate oxygen demands—primary intestinal epithelial cells (oxygen consuming) and *Bacteroides uniformis* (an anaerobic species prevalent in the human gut).

## 1. Introduction

In the body, cells consume oxygen diffusing from capillaries nearby and continuously regulate and respond to their oxygen microenvironment.<sup>[1]</sup> The oxygen microenvironment influences cellular and tissue functions of normal and disease states, where the local oxygen levels are defined by the pericellular oxygen concentration (POC) and intracellular oxygen concentration (IOC) (Figure 1a). In vivo, oxygen levels regulate diverse cellular activities and disease states, including stem-cell states,<sup>[2]</sup> stem-cell differentiation,<sup>[3]</sup> immune response in inflammation,<sup>[4,5]</sup> and pathogenesis of diseases such as cancer<sup>[6]</sup> and inflammatory bowel disease.<sup>[7]</sup> The oxygen microenvironment in local tissue is continuously and dynamically

C. Li, D. J. Beebe  
Carbone Cancer Center  
University of Wisconsin-Madison  
Madison, WI 53705, USA  
E-mail: cli479@wisc.edu; djbeebe@wisc.edu  
M. Humayun, J. Li, Y. Feng, H. Hefti, D. J. Beebe  
Department of Biomedical Engineering  
University of Wisconsin-Madison  
Madison, WI 53705, USA  
G. M. Walker  
Department of Biomedical Engineering  
University of Mississippi University  
Madison, MS 38677, USA

K. Y. Park  
Department of Surgery  
University of California San Francisco  
San Francisco, CA 94143, USA  
B. Connors, J. Feng, R. L. Clark, O. S. Venturelli  
Department of Biochemistry  
University of Wisconsin-Madison  
Madison, WI 53706, USA  
E-mail: venturelli@wisc.edu  
B. Connors, O. S. Venturelli  
Department of Chemical and Biological Engineering  
University of Wisconsin-Madison  
Madison, WI 53706, USA  
M. C. Pellitteri Hahn, C. O. Scarlett  
Analytical Instrumentation Center-Mass Spec Facility  
School of Pharmacy  
University of Wisconsin-Madison  
Madison, WI 53705, USA  
J. Schrope  
School of Medicine and Public Health  
University of Wisconsin-Madison  
Madison, WI 53726, USA

 The ORCID identification number(s) for the author(s) of this article can be found under <https://doi.org/10.1002/advs.202104510>

© 2022 The Authors. Advanced Science published by Wiley-VCH GmbH. This is an open access article under the terms of the Creative Commons Attribution License, which permits use, distribution and reproduction in any medium, provided the original work is properly cited.

DOI: 10.1002/advs.202104510

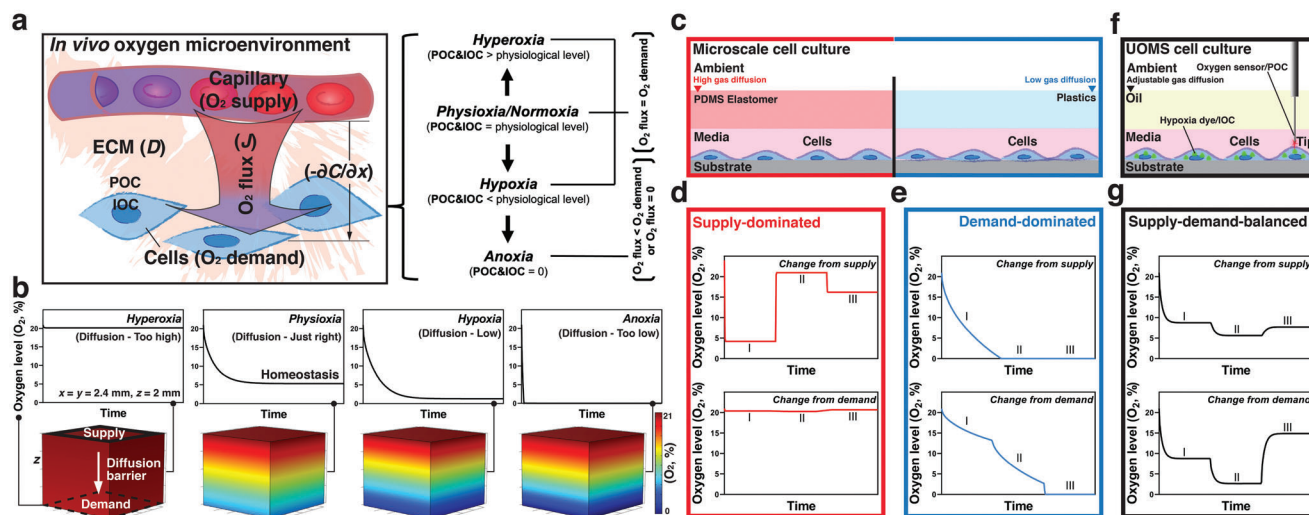


**Figure 1.** Numerical simulations of the typical oxygen microenvironments in in vivo and in vitro microscale cell culture systems. a) Schematic of a typical in vivo cellular and oxygen microenvironment. Oxygen levels including hyperoxia, physioxia (or normoxia), hypoxia, and anoxia are defined by POC and IOC relative to the physiological level of oxygen concentration in vivo (about 5%  $O_2$  on average). Hyperoxia, physioxia, or hypoxia is a result of homeostasis between  $O_2$  flux and  $O_2$  demand (i.e.,  $O_2$  flux =  $O_2$  demand). In cases where  $O_2$  flux is less than  $O_2$  demand, homeostasis cannot be reached, and the system ends up in anoxia. b) COMSOL Multiphysics results (Experimental Section) showing the typical kinetics of oxygen diffusion for different characteristic properties of diffusion barriers. Ambient oxygen level (21%  $O_2$ ) was set to diffuse from the supply (the top surface denoted by the black solid-line box, left-most inset) to the demand (the bottom surface denoted by the black dashed-line box, left-most inset). Model geometry was selected based on the dimensions of a standard 384 well (i.e.,  $x = y = 2.4$  mm), where the thickness of the diffusion barrier was set 2 mm (i.e.,  $z = 2$  mm). The walls of the model and the bottom surface were defined as gas impermeable. Oxygen level ( $O_2$ , %) measurements were obtained at the cell layer (i.e., the bottom surface). c) Schematic of a typical (closed-channel or closed-chamber) microscale cell culture system. The oxygen microenvironment in such microscale device is either supply-dominated (left), due to the high gas diffusivity of PDMS elastomer and small scale, or demand-dominated (right), where materials (e.g., PS or PMMA) with limited gas diffusivity are used. d, e) COMSOL Multiphysics results showing the typical kinetics of oxygen level at the cell layer against changes in oxygen supply or demand at three different stages (I, II, and III, Experimental Section) in a supply-dominated system (the red box) and a demand-dominated system (the blue box). A supply-dominated system is highly responsive to the change from supply (i.e., external settings of oxygen) but leaves the demand (i.e., oxygen consumption of cells) largely disconnected from regulating the oxygen microenvironment. By contrast, a demand-dominated system responds little to the change from supply and leads to anoxia (i.e., complete depletion of oxygen at the cell layer) and eventually to cell death. f) Schematic showing UOMS cell culture. Cells are cultured in media with an oil overlay: a proper diffusion barrier that allows mimicry of the supply–demand-balanced oxygen microenvironment as seen in vivo. For a given ambient and cell-media condition, gas diffusion through the oil overlay can be readily adjusted by selecting different oil properties (e.g., oil type, depth, viscosity). Enabled by the free physical access of UOMS, POC can be monitored with high spatial flexibility using an optical oxygen sensor that can be deployed directly onto the cell layers through the oil overlay. IOC is probed by a hypoxia dye (depicted as green triangles) in live cells. g) COMSOL Multiphysics results showing the typical kinetics of oxygen level at the cell layer in response to changes from the oxygen supply or demand in a supply–demand-balanced system (the black box). In response to these changes at each stage, a supply–demand-balanced system can reach a different level of homeostasis, autonomously.

regulated by a supply–demand balance. Homeostasis is achieved when oxygen ( $O_2$ ) flux from the supply (i.e., oxygen carried in capillaries) matches  $O_2$  demand of the cells through the diffusion barrier (i.e., extracellular matrix, or ECM), and changes in these parameters alter the oxygen microenvironment. In vivo, changes in  $O_2$  supply, for instance, can be caused by fluctuating blood flow in the chaotic and poorly hierarchical structure of tumor blood vessels.<sup>[8]</sup> Similarly,  $O_2$  demands can change during activation/repression of inflammation<sup>[9]</sup> or during a switch

between bioenergetic profiles.<sup>[10]</sup> For example, a hallmark of inflammation and many disease states is hypoxia caused by impaired supply and/or upregulated demand of oxygen relative to physiologically defined oxygen levels, also known as physioxia. For a given supply–demand balance, a Goldilocks or “just right” diffusion barrier is necessary to reach physioxia in the system (Figure 1b). In vivo, hypoxia or anoxia can also be caused by decreased tissue perfusion due to fibrosis.<sup>[11]</sup> These physiological/pathological changes cause variations in POC and IOC leading to aberrant oxygen levels that further elicit changes in cell function and cell-to-cell interactions.<sup>[12]</sup>

Compared to conventional, bulk-scale cell culture techniques (e.g., culture flasks), microscale cell culture (i.e., low volume ratio between media and cells with the media volume typically falling in the range of picoliters to microliters and commonly <1 mm of media depth) provides improved spatial and temporal control over many culture parameters,<sup>[13,14]</sup> allowing better mimicry of the dynamic and heterogeneous cellular microenvironment seen in vivo.<sup>[15,16]</sup> For instance, in vivo the cell-to-cell, cell-to-

O. S. Venturelli  
Department of Bacteriology  
University of Wisconsin-Madison  
Madison, WI 53706, USA

D. J. Beebe  
Department of Pathology and Laboratory Medicine  
University of Wisconsin-Madison  
Madison, WI 53705, USA

**Table 1.** Reported oxygen solubility and diffusivity of materials typically used in microscale cell culture systems.

Materials	Oxygen solubility (mL of gas/1 L of fluid @ 1 bar of air)	Diffusion coefficient of oxygen ( $\times 10^{-5} \text{ cm}^2 \text{ s}^{-1}$ @ 1 bar of air)
Deionized (DI) water	5.4 (37 °C) <sup>[29]</sup>	1.9–2.3 (25 °C) <sup>[30]</sup>
Typical cell culture media + 10% fetal bovine serum (FBS)	5.3 (37 °C) <sup>[31]</sup>	2.69 (37 °C) <sup>[31]</sup>
Silicone oil (SO)	51.9 (5 cSt, 38 °C) <sup>[32]</sup> Data not found (1000 cSt)	0.5 (500 cSt, 30 °C) <sup>[33]</sup> Data not found (5 cSt, 1000 cSt) (see Figure S2 in the Supporting Information)
Mineral oil	49.5 (hexadecane, 22 °C) <sup>[32]</sup>	2.49 (hexadecane, 22 °C) <sup>[32]</sup>
Fluorinert FC-40 (FC-40)	76.8 (25 °C) <sup>[32]</sup>	8.3 (22 °C) <sup>[32]</sup>
Polydimethylsiloxane (PDMS) elastomer	310 (27 °C) <sup>[34]</sup>	16 (27 °C) <sup>[34]</sup>
Polystyrene (PS)/polypropylene (PP)/polycarbonate (PC)	174.7 (PS, 25 °C) <sup>[35]</sup>	0.04–0.02 (25 °C) <sup>[36]</sup>
Polymethyl methacrylate (PMMA)	194.8 (25 °C) <sup>[35]</sup>	0.0025 (25 °C) <sup>[36]</sup>

environment interactions usually occur in a parenchyma (e.g., capillary bed) with a low volume ratio between interstitial fluid and cells, which defines the mass transport of various signaling factors (e.g., nutrients, vital gases, cytokines, etc.). Here, we aim to develop a method that allows the cells to regulate the oxygen microenvironment and respond to changes autonomously at microscale, via a supply–demand balance as seen in vivo.

Theoretically, the oxygen microenvironment in microscale cell culture systems can be regulated, through a diffusion barrier between the supply and demand, in three ways: supply-dominated, demand-dominated, and supply–demand-balanced (Figure 1c–g).<sup>[17]</sup> Various materials have been used to make microscale devices, including silicon, glass, plastic, and elastomer.<sup>[18]</sup> Among them, polydimethylsiloxane (PDMS) elastomer has been most frequently used. While commonly referred to as PDMS, the PDMS elastomer is essentially a porous, composite network of crosslinked polymer/oligomer, which is the PDMS, with various fillers/additives. Despite its wide acceptance, the ultrahigh gas diffusivity of PDMS elastomer (Table 1), combined with the small-scale nature of microscale cell culture systems [Figure 1c (left),d], render the oxygen microenvironment in PDMS-based systems supply-dominated. Oxygen levels in these systems are predominantly operator-defined and therefore, regulated by the supply, which means, for instance, by the ambient oxygen levels, via gas-regulating channels within PDMS devices, or by the continuous perfusion of oxygenated/deoxygenated media.<sup>[17]</sup> Change from the demand in a supply-dominated system has limited influence on the oxygen microenvironment. The supply-dominated oxygen microenvironment imposes an operator-defined concentration or gradient of oxygen level upon cells, which limits their spatiotemporal regulation and cellular response to the oxygen microenvironment in a physiolog-

ically relevant manner. By contrast, gas-impermeable plastics such as polystyrene (PS) and polymethyl methacrylate (PMMA) have been used to block oxygen diffusion into microscale cell culture chambers (Table 1).<sup>[19]</sup> The oxygen microenvironment in these systems are demand-dominated [Figure 1c (right),e], i.e., predominantly defined by oxygen consumption of the cells within the system with limited supply regulation. Without continuous replenishment of oxygen supply (e.g., static media in sealed microwells),<sup>[20]</sup> the demand-dominated oxygen microenvironment results in continuous decrease in oxygen levels to hypoxia and eventually to anoxia that leads to cell death. To mimic the kinetics and spatiotemporal variations in oxygen tensions characteristic of in vivo biology, cell culture systems should accommodate a Goldilocks or “just right” diffusion barrier for a supply–demand-balanced oxygen microenvironment as opposed to a strictly supply-dominated or demand-dominated system. The supply–demand-balanced oxygen microenvironment allows continuous and dynamic regulation of the oxygen levels (i.e., POC and IOC) and cellular response via a supply–demand balance (Figure 1f,g).

Recently, there has been renewed interest in the area of multi-liquid-phase microfluidics, known as under-oil open microfluidic systems (UOMS).<sup>[21–28]</sup> In UOMS cell culture, culture media and cells are contained under an oil overlay, separating the cell culture microenvironment from the ambient with an immiscible liquid (i.e., oil) rather than solid materials used in traditional microscale devices (Figure 1f; Figure S1, Supporting Information). Thus, compared to PDMS elastomer or other solid materials used in closed-channel or closed-chamber microscale devices, the oil overlay allows: i) integration of a readily tailorable diffusion barrier for a supply–demand-balanced oxygen microenvironment by selecting/adjusting different oil properties (e.g., oil type, depth, and viscosity), and ii) facile and seamless intervention and spatially flexible deployment of external sensors (e.g., oxygen, pH, temperature, and etc.) on the device to monitor the culture microenvironment in real time.

In this work, we demonstrate the establishment and monitoring of AROM in UOMS cell culture via a supply–demand balance, covering a full range of oxygen levels, including hyperoxia, physioxia, hypoxia, and anoxia. Using oil overlay, AROM can be achieved without the need to vary the media volume (i.e., the volume ratio between media and cells) and the media depth, which simultaneously changes cellular physiology and metabolism (e.g., nutrient availability, signaling efficiency). Moreover, AROM does not require media pre-deoxygenation (i.e., complete depletion of oxygen dissolved in the culture media) or external gas-regulating equipment, which streamlines the operation and lowers the adoption barrier among end users. We calculate the kinetics of oxygen diffusion against varying supply, demand, and diffusion barriers using COMSOL Multiphysics. For experimental validation, a panel of cell types including various mammalian cells (epithelial, endothelial, stromal, immune), fungi, and bacteria are examined to assess their capacity to regulate the oxygen microenvironment under oil. A key challenge in in vitro modeling at the microscale is establishing cocultures of oxygen-consuming human intestinal epithelium and anaerobic commensal bacteria that inhabit the gastrointestinal tract, due to their disparate oxygen demands. We apply the method described in this manuscript to establish and characterize a cocul-

ture of human primary intestinal epithelial cells and *Bacteroides uniformis* (*B. uniformis*), a highly prevalent human-associated intestinal species, with these complex oxygen demands.

## 2. Results and Discussion

### 2.1. Numerical Simulation of the Kinetics of Oxygen Diffusion in Multi-Liquid-Phase Microsystems

We first establish conceptually the kinetics of oxygen transport within a microscale, multi-liquid-phase culture system to provide general guidance for establishing AROM using different materials (e.g., culture media, plastic, elastomer, oil). The kinetics of oxygen diffusion in a microsystem (flow-free) can be quantitatively described using Fick's laws. Fick's first law describes  $O_2$  flux ( $J$ ) (i.e., mass transport of oxygen per unit time per unit area) as

$$J = -D(\partial C/\partial x) \quad (1)$$

where  $D$  is the diffusion coefficient of the diffusion barrier,  $\partial x$  is the distance between the supply and the cells,  $-dC$  is the difference in oxygen concentration between the supply and the cells, and  $-\partial C/\partial x$  is the oxygen gradient (Figure 1a).

When  $O_2$  flux matches  $O_2$  demand, which can be defined by:  $O_2$  demand = oxygen consumption rate (OCR) (i.e., the amount of oxygen consumed per cell per unit time)  $\times$  cell density (i.e., cells per unit area), the system reaches a supply–demand balance or oxygen homeostasis. The oxygen homeostasis can be shifted by changes from supply and/or demand (Figure 1g). For instance, higher oxygen supply results in increased POC and consequently IOC, whereas higher oxygen demand by cells results in decreased IOC and thereby a decrease in POC. Fick's second law describes the change in oxygen concentration over time ( $\partial C/\partial t$ )

$$\partial C/\partial t = D\partial^2 C/\partial x^2 \quad (2)$$

For a given  $\partial^2 C/\partial x^2$ , the inherently large gas diffusivity (i.e.,  $D$ ) in PDMS-based microdevices results in a large  $\partial C/\partial t$ . Therefore, the large  $D$  and  $\partial C/\partial t$  together result in the supply-dominated nature in the PDMS-based microdevices (i.e., high responsivity of POC and IOC to changes from supply), allowing little change in  $-\partial C/\partial x$  [the oxygen gradient established between the supply (i.e., either the ambient, gas-regulating channels, or the culture media) and the cells] when there is an altered  $O_2$  demand in the cells [Figure 1c (left),d]. Hence, in supply-dominated systems an altered  $O_2$  demand of the cells has little influence on POC and IOC, limiting relevance to the in vivo oxygen microenvironments where cells define the  $O_2$  demand, regulate the oxygen levels (i.e., POC and IOC), and respond to the oxygen microenvironment [e.g., via the hypoxia-inducible factor (HIF) signaling pathways]<sup>[6,12]</sup> in a real-time feedback loop. By contrast,  $O_2$  flux is negligible (i.e.,  $J \rightarrow 0$ ) in demand-dominated systems due to the limited gas diffusivity (i.e.,  $D \rightarrow 0$ ), and thus oxygen in the media is continuously depleted by the cells and eventually leads to anoxia (i.e., POC and IOC = 0%  $O_2$ ) and cell death [Figure 1c (right),e].

Using numerical simulation (Experimental Section), we first analyze the influence of media depth on the kinetics of oxygen

diffusion (Figure 2a,b). As expected, if the media depth is too small (<1 mm), little decrease of oxygen level is obtained. By simply increasing the media volume and thus the depth, the full range of oxygen levels (i.e., hyperoxia, physioxia, hypoxia, and anoxia) can be achieved. However, increasing cell culture volume increases the volume ratio between media and cells, thereby changing the biology of the system and compounding the parameter space. In comparison, an oil overlay provides an effective and flexible approach to achieve supply–demand-balanced oxygen microenvironments in microscale cell culture without changing the volume ratio between media and cells.

In typical UOMS cell culture, mineral (or paraffin) oil, silicone oil [i.e., pure linear PDMS polymer liquid (without small molecule additives and crosslinkers)], and fluorinated oil (i.e., perfluorocarbon liquid) are the three most commonly used oil types due to their overall biocompatibility.<sup>[37]</sup> However, in the context of gas permeability, the properties of oxygen solubility and diffusivity vary considerably among these oil types (Table 1). For instance, fluorinated oil has notably high oxygen solubility and diffusivity, and has been previously used as an oxygen carrier (i.e., to increase oxygen delivery) in cell culture.<sup>[32]</sup> In comparison, oxygen solubility and diffusivity of silicone oil (which is viscosity-dependent) can be significantly lower than fluorinated oil. To control oxygen diffusion through the oil overlay we selected silicone oil as the gas diffusion barrier for achieving AROM in UOMS cell culture. Moreover, silicone oil also allows exclusive liquid repellency (ELR): an extreme wettability in which a liquid is absolutely repelled from a solid surface when exposed to a proper secondary immiscible liquid. ELR enables versatile and advanced control of open fluids which has been reported in our previous UOMS publications.<sup>[23,25,38]</sup>

Furthermore, we perform the simulation with oil overlay for two cell seeding densities (i.e.,  $1 \times 10^4$  cells well<sup>-1</sup> vs  $3 \times 10^4$  cells well<sup>-1</sup>) against two oil types (i.e., fluorinated oil vs silicone oil), and two different viscosities of silicone oil (i.e., 5 cSt vs 500 cSt) (Figure 2c–f). For a given volume ratio between media and cells, higher viscosity of silicone oil leads to lower oxygen levels (Figure 2d), which is consistent with the oxygen diffusion test results (Figure S2, Supporting Information). Due to its high gas diffusivity, fluorinated oil does not act as a significant diffusion barrier to oxygen when overlaid above the culture media layer (Figure 2b,e). In comparison, silicone oil shows a more significant influence on oxygen diffusion, and thus the oxygen levels (Figure 2f).

While not the focus of this work, we also investigate the oxygen diffusion in PDMS-based microscale culture systems, i.e., through PDMS elastomer layers with a small media depth (e.g., 0.25 mm) (Figure 2g–k). The simulations show that the PDMS elastomer layer has little influence on oxygen diffusion within a reasonable device-layer thickness (e.g., below 100  $\mu$ m) (Table 1; Figure 2h). We then seek to examine the influence of oil overlay on the oxygen microenvironment of cell culture within a PDMS-based device. To achieve this, we overlaid silicone oil on top of the PDMS-based devices. It is worth noting that silicone oil causes severe swelling of PDMS-based devices, whereas fluorinated oil, due to its chemical inertness, does not have this effect on PDMS elastomer. As fluorinated oil is not a significant diffusion barrier (Figure 2j), we implemented a silicone oil plus fluorinated oil, the so-called “double-oil” overlay setup. Using double-oil overlay, especially with high viscosity of silicone oil, effects of silicone oil on

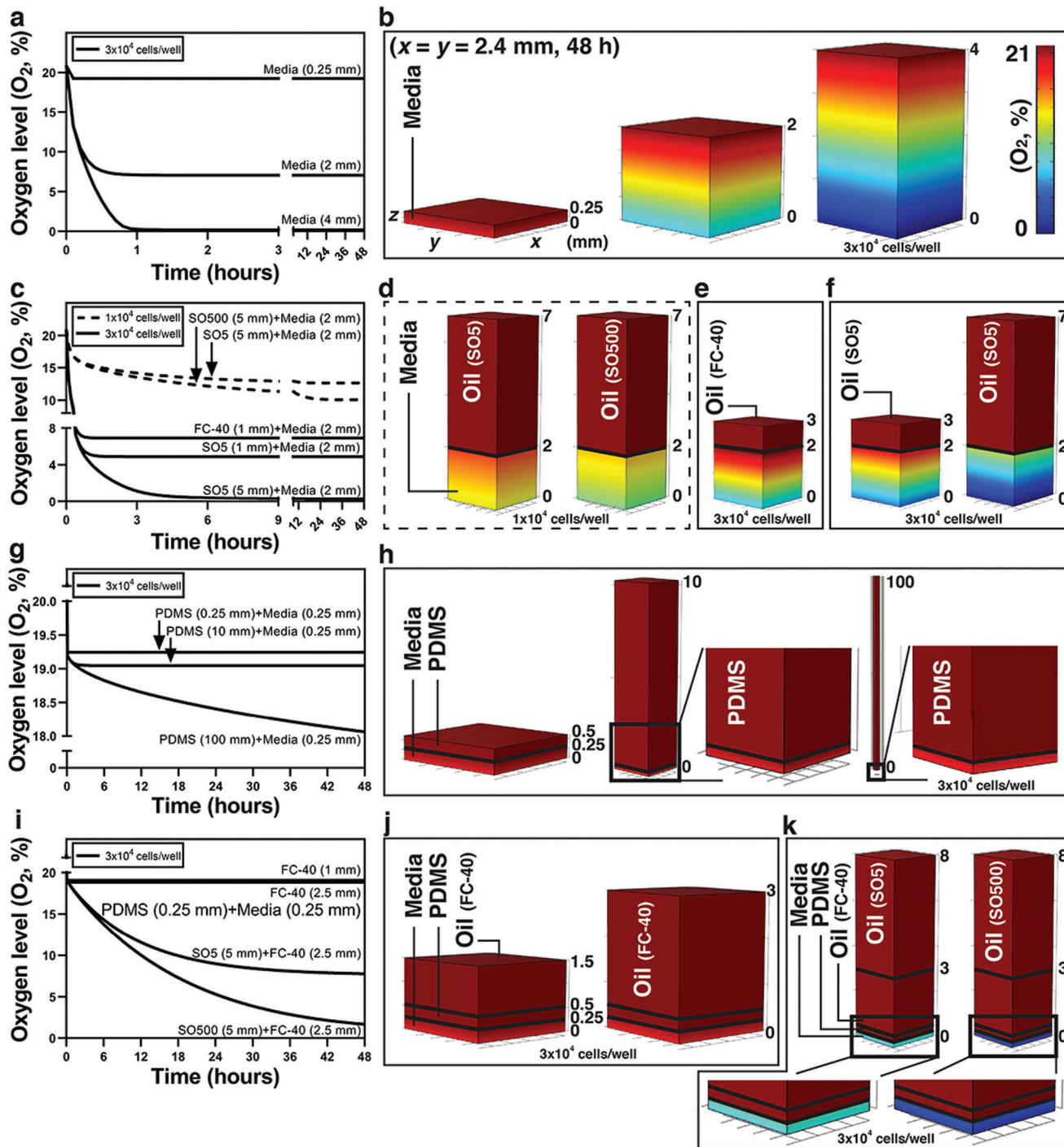


**Figure 2.** COMSOL Multiphysics results of the kinetics of oxygen diffusion in multi-liquid-phase microsystems and 3D diffusion profiles. a,b) Plots of oxygen levels ( $O_2$ , %) over time and 3D diffusion profiles at the cell layer in response to changes in media depth. c–f) Plots of oxygen levels ( $O_2$ , %) over time and 3D diffusion profiles in response to changes in oil type [fluorinated oil (FC-40) vs silicone oil (SO)], depth, and viscosity [5 cSt (SO5) and 500 cSt (SO500) of silicone oil]. g) and h) Plots of oxygen levels ( $O_2$ , %) over time and 3D diffusion profiles in PDMS (elastomer)-based microdevices. i–k) Plots of oxygen levels ( $O_2$ , %) over time and 3D diffusion profiles in PDMS (elastomer)-based microdevices with oil (i.e., fluorinated oil) or double-oil (i.e., fluorinated oil + silicone oil) overlay. The color legend of oxygen shown in (b) is defined based on the oxygen level in the media phase and thus the oxygen gradient in the media phase can be better visualized. 21%  $O_2$  on the color legend corresponds to oxygen solubility of (or oxygen-saturated) media (Table 1).

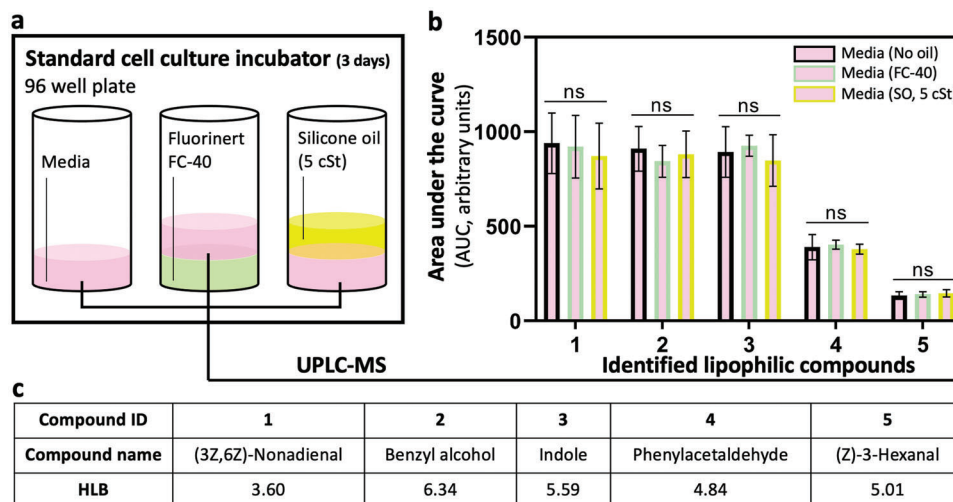


**Figure 3.** UPLC-MS media analysis for the retention of lipophilic molecules in UOMS cell culture. a) Schematic showing three conditions tested, where culture media was incubated alone, with fluorinated oil (Fluorinert FC-40), and with silicone oil (SO, 5 cSt) overlay for 3 days [at 37 °C, 18.6% O<sub>2</sub>, 5% carbon dioxide (CO<sub>2</sub>), and 95% relative humidity (RH)] without agitation before collection and analysis. b) Comparison of the relative abundance (i.e., area under the curve, or AUC from the extracted ion chromatograms, or EICs) (see Figure S4 in the Supporting Information) of five identified lipophilic compounds found in a commonly used culture media. “ns” represents “not significant.” c) The compound names in (b) with the HLB values.

the oxygen levels in PDMS-based microscale devices (Figure 2k) can be retained. These simulation results were further validated in experiments (Figure S3, Supporting Information).

## 2.2. Investigating the Retention of Lipophilic Molecules in UOMS Cell Culture

A frequently expressed concern during the development of UOMS cell culture is the possible extraction of lipophilic molecules by the oil phase from the culture media. We believe this is an important attribute of the system that needs to be carefully inspected and understood before its use in cell cultures. The general biocompatibility of silicone oil in cell culture has been proven and reported. Here, we use ultra-performance liquid chromatography-tandem mass spectrometer (UPLC-MS) to systematically analyze possible molecule loss in UOMS cell culture (Figure 3; Figure S4, Supporting Information).

We examined extraction of lipophilic molecules in a typical culture media [Dulbecco’s Modified Eagle’s medium (DMEM) + 10% FBS + 1% Pen-Strep] incubated in a standard polystyrene 96-well plate under standard cell culture environment (Figure 3a, Experimental Section). The media was collected and analyzed on UPLC-MS after 3 days of incubation without agitation of the oil and media layers. The identified molecules from UPLC-MS were ranked by their hydrophilic–lipophilic balance (HLB) values. The top five lipophilic molecules with HLB ranging from 0 to about 6 (Figure S4, Supporting Information) were selected for comparison between the no oil and oil conditions (Figure 3b,c). Fluorinated oil shows no molecule loss like the no oil condition, due to its widely reported chemical inertness. Most importantly, we did not observe any significant molecule loss from silicone oil either. The retention of small molecules in water-in-oil emulsion droplets has been broadly studied in droplet microfluidics.<sup>[39]</sup> In general, the molecule retention or loss depends highly on the

lipophilicity of the target molecule and the surfactant layer (i.e., surfactant type and concentration) at the oil–media interface (Figure S5, Supporting Information). It has been reported that the addition of biopolymers (e.g., bovine serum albumin, or BSA) significantly improves the retention of lipophilic molecules in the media phase.<sup>[40]</sup> It’s worth noting that how the gaseous-phase signaling molecules such as nitric oxide (NO) and nitrous oxide (N<sub>2</sub>O) might be affected by the surfactant layer and the different oil phases and thus how it may influence cell function remain unclear from this work and require a systematic study. The high retention of lipophilic molecules in the culture media from the UOMS cell culture narrows down the parameter space and control conditions that affect cell response in cell culture and cell-based assays.

## 2.3. Kinetics of POC and IOC in UOMS Cell Culture with Varying Supply–Demand Balances

The oxygen microenvironment in vivo is highly heterogeneous across organs.<sup>[1]</sup> In local tissue, the POC and IOC vary spatially between the cells and the supply (i.e., capillaries), and are precisely defined by the supply–demand balance. For example, a steep oxygen gradient is known to exist in the intestine where 4–8% O<sub>2</sub> is observed in the submucosa and lamina propria, 2–4% across the epithelial and mucous layer, and less than 2% in the lumen.<sup>[7]</sup> We chose a representative cell line of the intestinal tissue (human colorectal tumor cell line, Caco-2) to demonstrate the capability of UOMS cell culture via AROM to recapitulate different local oxygen levels of tissue in vivo (Figure 4a,b). The POC in UOMS cell culture can be monitored at any point of time and location by directly introducing single or multiple external oxygen microsensors through the oil overlay. To facilitate dynamic monitoring of the kinetics of oxygen levels with single-cell resolution, we used a hypoxia dye taken up by live cells to probe the

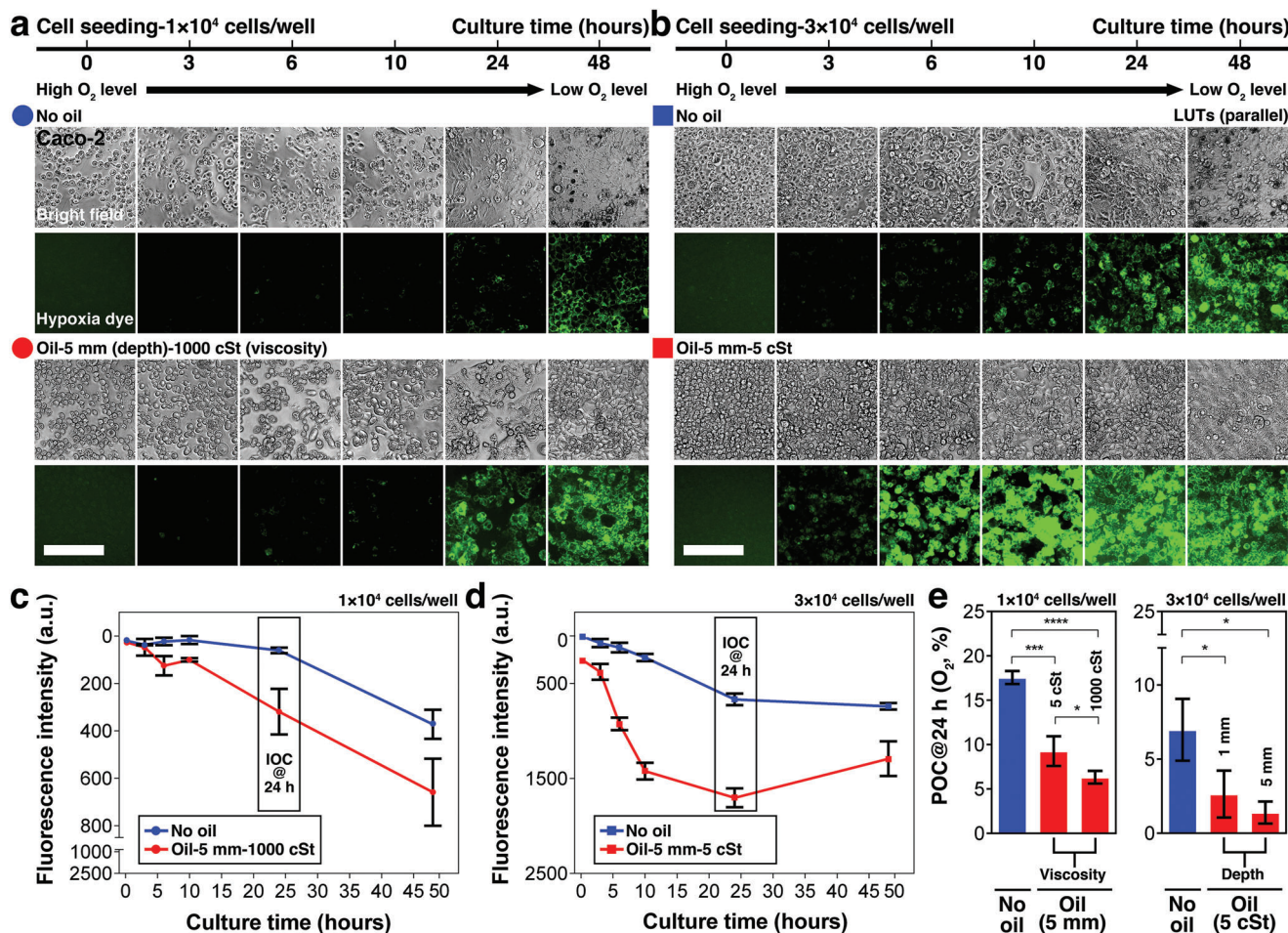


**Figure 4.** Kinetics of POC and IOC in UOMS cell culture with different cell seeding densities and select oil properties. Intestinal epithelium cell line (Caco-2) was cultured at two different seeding densities with and without oil overlay: a)  $1 \times 10^4$  cells well $^{-1}$ , and b)  $3 \times 10^4$  cells well $^{-1}$  leads to a near-confluent monolayer from cell seeding in a standard 384 well. The volume of media was set at a constant  $20 \mu\text{L well}^{-1}$  (for  $2 \text{ mm}$  media depth).  $10$  or  $50 \mu\text{L well}^{-1}$  of silicone oil ( $5 \text{ cSt}$  or  $1000 \text{ cSt}$ ) was added on top of the media layer (for an additional  $1$  or  $5 \text{ mm}$  in oil depth). The fluorescent images of hypoxia dye were processed with parallel lookup tables (LUTs) (i.e., the same minimum and maximum in brightness/contrast adjustment) for the comparison of fluorescence intensity. See Figure S7 (Supporting Information) for large images of the typical cell morphologies. Scale bars,  $200 \mu\text{m}$ . c, d) The kinetics of IOC (monitored by the hypoxia dye) in  $48 \text{ h}$  corresponding to (a) and (b), respectively. e) The influence of oil viscosities ( $5 \text{ cSt}$  vs  $1000 \text{ cSt}$ ) or depths ( $1 \text{ mm}$  vs  $5 \text{ mm}$ ) shown by POC ( $O_2$ , %) measured at  $24 \text{ h}$  using the optical oxygen sensor (Figure S1, Supporting Information). Data were pooled and averaged with 3 replicates in each condition. Error bars, mean  $\pm$  s.d. \* $p \leq 0.05$ , \*\* $p \leq 0.01$ , \*\*\* $p \leq 0.001$ , and \*\*\*\* $p \leq 0.0001$ .

IOC in parallel with the POC measurements. The combined POC and IOC measurements (Experimental Section) allow a reliable and multifaceted way to monitor the oxygen microenvironment in UOMS cell culture.

Here, we compare the trends of our previously simulation results (Figure 2) of the kinetics of oxygen diffusion with experimental results. We examine the influence of cell seeding density and oil properties (i.e., oil depth and viscosity) on POC and IOC of cells cultured in UOMS with AROM.

The following guidelines were established prior to interpreting our experimental results. In this study, we ensured cell culture media was normally saturated with oxygen from exposure to atmospheric concentration (i.e.,  $21\% O_2$ ). Immediately after cell seeding,  $O_2$  flux is assumed to be zero (i.e.,  $J = 0$ ) as no oxygen gradient has yet been established (i.e.,  $-\partial C/\partial x = 0$ ). Over time,

$O_2$  flux will increase (i.e.,  $J > 0$ ) as cells consume the dissolved oxygen from the surrounding media, thereby establishing an oxygen gradient that increases the difference between ambient and the local media (i.e.,  $-\partial C/\partial x > 0$ ). Eventually,  $O_2$  flux reaches its maximum, either determined by (and equal to)  $O_2$  demand or less than the demand, at which point diffusion becomes the rate-limiting step. In cases where  $O_2$  flux matches  $O_2$  demand, POC and IOC reach a steady state (or homeostasis). In cases where  $O_2$  flux is less than  $O_2$  demand (i.e., inadequate oxygen delivery to the cells), POC and IOC drop to  $0\% O_2$ , which leads to anoxia. For simplicity, we assume a constant  $O_2$  demand, and note that  $O_2$  demand may vary over time due to cell proliferation, cell death, or changes in metabolic activities. To achieve a quasi-constant  $O_2$  demand (e.g., within  $24 \text{ h}$  of culture), we chose the seeding density of  $3 \times 10^4$  cells well $^{-1}$  which produces a near-confluent mono-

layer of cells in a standard 384 well. In such conditions, cell proliferation is not a dominant parameter that significantly varies  $O_2$  demand due to contact inhibition and limited surface area. To investigate the influence of cell growth on the kinetics of AROM, we used a lower seeding density ( $1 \times 10^4$  cells  $well^{-1}$ ) to compare in parallel. In all tested conditions, cell viability was maintained at a normal level (Figure S6, Supporting Information). Our results indicate that the conditions with larger volume ratio between media and cells and/or oil overlay exhibited higher cell viability.

Here, we demonstrate that our experimental results captured the simulated kinetics of oxygen diffusion over a period of 48 h as described above. We summarize here several observations that can be used as guidelines to understand and control the kinetics of AROM in UOMS cell culture:

- i) Higher cell seeding density or larger oil depth/viscosity leads to lower POC and IOC (Figure 4c–e).
- ii) For the default cell seeding density (i.e.,  $3 \times 10^4$  cells  $well^{-1}$  in a standard 384 well) and cell type (i.e., Caco-2), POC and IOC reach a steady state (or homeostasis) in around 24 h from the initiation of culture (Figure 4d). It takes a longer time for the oxygen microenvironment to reach homeostasis with lower  $O_2$  demand (e.g., lower cell seeding density or a cell type with lower OCR) (Figure 4c).
- iii) Varying the oil depth in the cultures with a confluent monolayer of Caco-2 cells (the  $3 \times 10^4$  cells  $well^{-1}$  condition) created oxygen levels representative of different regions of the intestine: the submucosa (no oil overlay,  $\approx 7\% O_2$ ), epithelial and mucous layer (1 mm oil overlay,  $\approx 3\% O_2$ ), and lumen (5 mm oil overlay,  $< 2\% O_2$ ) (Figure 4e, right).
- iv) We noticed the following trend in regard to error bars in our IOC and POC measurements: iv–i) On the IOC plots (Figure 4c,d), the error bars from the later time points become noticeably larger compared to the early time points. This trend can be also identified in the fluorescent images of the hypoxia dye (Figure 4a,b). Defined by the nature of the hypoxia dye (Experimental Section), the heterogeneity of the fluorescence signal of the hypoxia dye increases over time, which reflects the local heterogeneity of uptake of the dye by cells and/or IOC at the single-cell level. This heterogeneity may contribute to the overall IOC measurement of the entire well. iv–ii) However, we observed the reversed trend in the POC measurements. On the POC plots (Fig. 4e), the error bars from the condition with high cell seeding density are larger than from low cell seeding density, especially for the early time points. This can be attributed to the uneven distribution of cells in a well from cell seeding. Such unevenness can be more often seen with increased seeding density. Over time with the decreased oxygen level in a well, the difference of POC caused by the uneven distribution of cells decreases, which leads to smaller error bars.
- v) Different oxygen levels (Figure 1a) can be obtained without using oil overlay, for example, by only changing the media depth<sup>[31]</sup> (Figures 2a and 4e; Figure S8, Supporting Information). However, as previously mentioned, the change of media volume in a culture also changes many other factors such as nutrient availability and the concentration of metabolites or signaling molecules that together compound the readouts.

Taken together, the results validate the high flexibility and controllability of establishing AROM in UOMS cell culture with a proper oil overlay.

#### 2.4. Cellular Regulation of the Under-Oil Oxygen Microenvironment

A typical in vivo cellular microenvironment includes multiple cell types, and in many cases inter-kingdom interactions. It is well known that a broad heterogeneity of OCR exists across cell types.<sup>[31]</sup> Here, a panel of mammalian and fungal cell types (Figure S9 and Table S1, Supporting Information) are examined for their capacity to regulate the oxygen microenvironment in UOMS cell culture. This test also demonstrates the capability to achieve compartmentalization and high-throughput oxygen regulation in a single device that is exposed to the same environment (e.g., ambient, or standard incubator conditions) (Figure 5a).

Within the cohort of mammalian cells, cancer cell lines [Caco-2 (a human colorectal adenocarcinoma),<sup>[41]</sup> MDA-MB-231 (a migrating breast cancer)<sup>[42]</sup>], and endothelial cells [human umbilical vein endothelial cell (HUVEC)<sup>[43]</sup>] show high OCR according to both POC and IOC measurements (Figure 5b). In comparison, fibroblasts [CAF (cancer-associated fibroblasts, breast cancer tissue), colon fibroblasts (normal tissue)] and the two types of nonadherent white blood cells [THP-1 (a human monocytic cell line) and neutrophils (primary)]<sup>[44]</sup> show a relatively lower OCR compared to other cell types. The fungus (*Candida albicans*, or *C. albicans*) dwarfs all the mammalian cells with respect to a drop in POC and IOC levels due to its rapid growth rate and high OCR<sup>[45]</sup> relative to mammalian cells. It is worth noting that the POC and IOC levels for each cell type examined in UOMS cell culture are consistent with reported OCRs and the typical bioenergetic profiles taken by those cell types.<sup>[41–45]</sup> In UOMS cell culture, we use oxygen-saturated (i.e., 21%  $O_2$ ) media to start a culture. With a given culture condition, including cell seeding density, volume ratio between media and cells, and an oil overlay, cells with high OCR allow a large range of POC and IOC from monoculture of the cells within a practical range of time, e.g., 24 h. This property is defined as high capacity of oxygen regulation. By contrast, cells with low OCR show limited capacity of oxygen regulation. Indeed, in a cellular microenvironment involving multiple cell types, the OCR of individual cell types may change via cell-to-cell signaling or crosstalks. Systematically examining the influence of the signaling factors on OCR in combinatorial cocultures is beyond the scope of this investigation. The results in this section provide a basis for the capacity of oxygen regulation of each cell type prior to establishing inter-kingdom coculture systems with AROM.

In vivo, the oxygen microenvironment is dynamically regulated and reconditioned as the supply–demand balance shifts in response to various stressors. Here, we seek to demonstrate reconditioning of the AROM in UOMS cell culture that mimics the in vivo oxygen homeostasis processes. We adopted a standard mitochondrial stress assay kit to manipulate the mitochondrial respiration, and thus the OCR (or  $O_2$  demand) of the cells (Experimental Section) (Figure 5c). The POC of the UOMS cell culture was monitored in real time for 3 h (Figure 5d). The results showed a fast and robust response of the AROM to the mi-



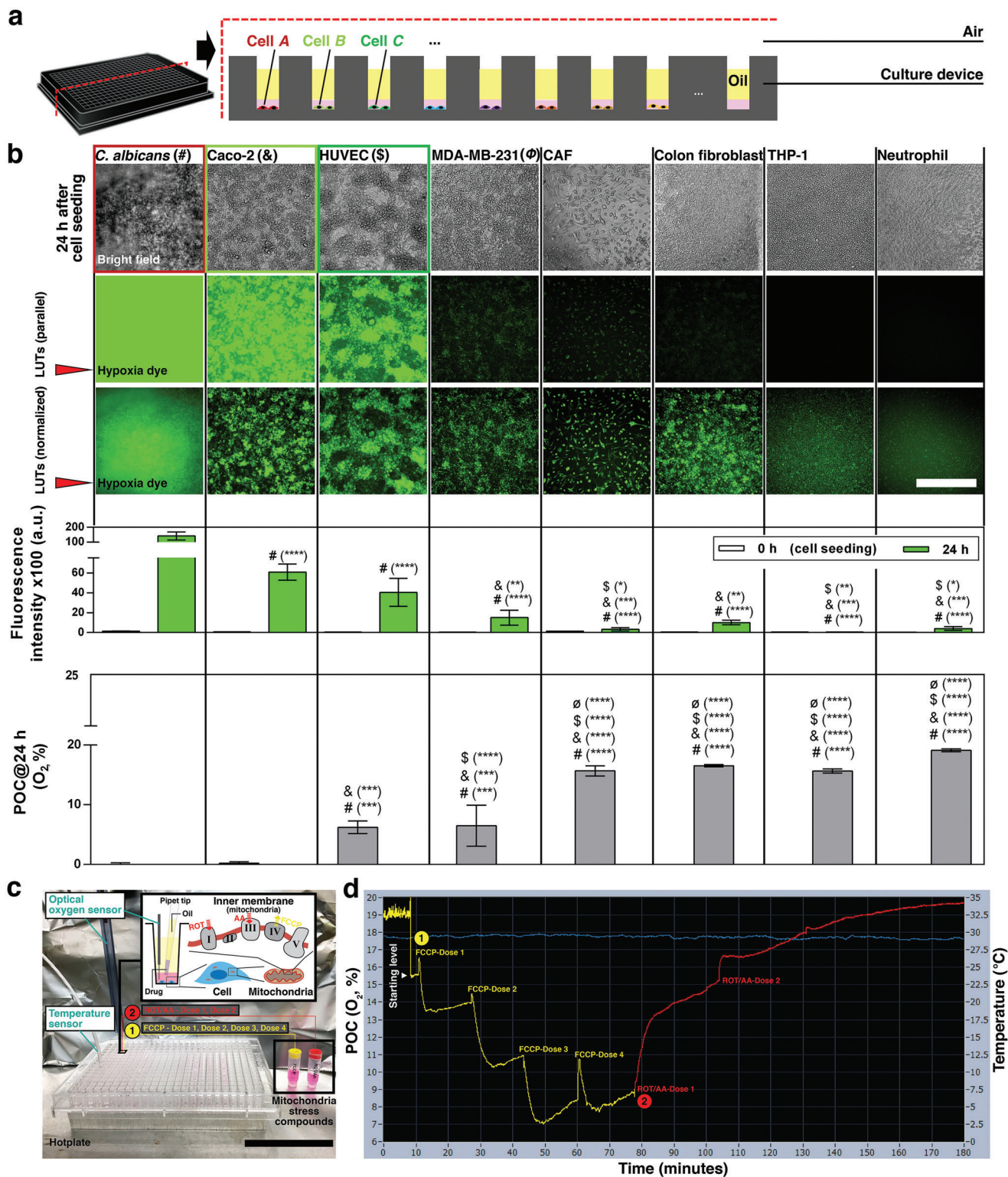


**Figure 5.** Under-oil oxygen microenvironments regulated by different cell types and controlled bioenergetic states. a) Schematic showing the compartmentalization and high-throughput oxygen regulation (in one 384-well plate) with different cell types and a shared atmosphere (e.g., air). b) Each cell type was seeded at  $3 \times 10^4$  cells well<sup>-1</sup> on a 384-well plate with 20  $\mu$ L well<sup>-1</sup> of media (for 2 mm in media depth), overlaid with 50  $\mu$ L well<sup>-1</sup> of silicone oil (5 cSt) (for an additional 5 mm in oil depth), and cultured up to 24 h for a parallel comparison. The fluorescent images of hypoxia dye were processed with parallel LUTs (the middle row) for the comparison of fluorescence intensity, and with normalized LUTs (i.e., individually adjusted minimum and maximum in brightness/contrast) (the bottom row) for visualization. See Figure S10 (Supporting Information) for large images of the typical cell morphologies. Scale bar, 500  $\mu$ m. The bar graph of POC (O<sub>2</sub>, %) and IOC (fluorescence intensity of hypoxia dye) of each cell type is displayed under relevant

tochondrial stress compounds with a series of reconditioned oxygen levels (i.e., the characteristic supply–demand-balanced oxygen response and homeostasis shown in Figure 1g) successfully captured.

## 2.5. Establishing a Coculture between Primary Colon Epithelial Cells and Human-Associated Anaerobic Intestinal Bacteria Using UOMS Cell Culture

A major challenge in studying biological systems is the development of coculture models that can recapitulate key parameters of natural microenvironments.<sup>[46]</sup> In this section, we explore an in vitro coculture between intestinal epithelium and anaerobic bacteria, which presents unique challenges due to their distinct demands for and tolerance of oxygen. A specific oxygen microenvironment must be established to sustain metabolic activities of host cells and bacteria with physiological or pathological relevance. While several in vitro coculture models have been developed to study host-microbe interactions utilizing microscale cell culture,<sup>[47,48]</sup> the oxygen levels in these systems are typically supply-dominated (or demand-dominated) as previously discussed, imposing a physiologically inconsistent oxygen microenvironment to the cells. In addition, the adoption barrier of these in vitro models, including limited access to samples within the devices due to the closed-channel or closed-chamber designs as well as limited access to specific equipment for device fabrication and operation, have stymied their broader adoption. Here, we apply the UOMS cell culture with AROM to establish a coculture between primary colon epithelial cells and human-associated anaerobic intestinal bacteria. We characterize and validate the coculture using measurements of POC, gene and protein level expression of differentiation markers of the intestinal epithelium, and bacterial growth.

Although investigators have traditionally relied on colon cancer cell lines to study gut epithelial physiology, they may possess nonphysiologic characteristics including altered metabolism, and aberrant proliferative and differentiation characteristics which call into question their predictive ability in modeling normal epithelial function.<sup>[49,50]</sup> In this coculture experiment, we cultured monolayers of colon epithelium derived from primary tissue on a thin layer of ECM coated culture plate (Figure 6a, Experimental Section) to represent a more physiologically relevant cellular microenvironment. Colon monolayers were overlaid with oil for 24 h to establish AROM prior to inoculation with anaerobic bacteria. Immunofluorescence staining (IFS) of E-cadherin and ZO-1 confirmed formation of epithelial adherens junction,

and z-stack modeling was used to determine monolayer formation (Figure 6b; Figure S11 and Table S2, Supporting Information) in the UOMS cell culture. In the gut, intestinal stem cells differentiate into specialized cell types, including absorptive enterocytes and mucus-producing goblet cells which make up the intestinal epithelium separating the gut lumen from the underlying parenchyma.<sup>[51]</sup> In our UOMS cell culture, IFS of colon monolayers further confirmed expression of cell lineage markers such as mucin 2 (goblet cells), FABP1 (enterocyte), and villin (enterocytes expressing microvillar actin-binding protein) (Figure S11, Supporting Information), indicative of a differentiated epithelium. Qualitative assessment of the IFS data showed no significant differences between the control (i.e., no oil overlay) and the AROM conditions (i.e., oil overlay) indicating biocompatibility of the oil overlay (silicone oil) in the in vitro culture of primary cells.

The adult intestinal microbiota consists of hundreds of species, the majority being obligate anaerobes, which are inhibited by the presence of oxygen due to their inability to defend against cellular damage by reactive oxygen molecules.<sup>[52]</sup> In the colon, oxygen is consumed by luminal components and the resident tissue cells to maintain the growth of strict anaerobes.<sup>[7]</sup> We hypothesized that by leveraging AROM by primary intestinal epithelial cells in UOMS cell culture, the oxygen level can be reduced to the physiological level that facilitates the coculture and growth of strict anaerobes such as *Bacteroides*. *Bacteroides* are a highly prevalent and abundant group of species in the human gut microbiome that can benefit the host by performing chemical transformations that provide key nutrients to the host.<sup>[53]</sup> In general, *Bacteroides* are strict anaerobes but specific species such as *B. fragilis* have been shown to tolerate and benefit from nanomolar oxygen.<sup>[54]</sup> Here, we used *B. uniformis*, genetically modified to constitutively express mCherry fluorescent protein (mCherry) to demonstrate the utility of our method in facilitating the coculture of primary intestinal cells with human-associated anaerobic bacteria. POC measurements of the colon monolayer [Figure 6c, colon (no oil/oil)] showed that with the oil (silicone oil, 5 cSt) overlay the oxygen level can be autonomously reduced to 2–8%, consistent with the physioxia of intestinal tissue, compared to no-oil controls where oxygen levels remained at hyperoxia (17–19% O<sub>2</sub>). The reduced oxygen level from the under-oil culture elicited upregulation of the HIF-1 $\alpha$  and HIF-2 $\alpha$  expression (Figure S12, Supporting Information), showing the response of the cells to the changed oxygen microenvironment. To investigate the OCR of *B. uniformis*, POC measurements of *B. uniformis* monocultures were performed with and without oil overlay. Despite the oil over-

panels of the fluorescent images. Data were pooled and averaged using 2 separate cell passages and with a minimum of 3 replicates for each condition. Error bars, mean  $\pm$  s.d. \* $p \leq 0.05$ , \*\* $p \leq 0.01$ , \*\*\* $p \leq 0.001$ , and \*\*\*\* $p \leq 0.0001$ . c) Experimental setup for regulation of mitochondrial respiration and reconditioning of oxygen microenvironments in UOMS cell culture. Caco-2 cells [ $1 \times 10^4$  cells well<sup>-1</sup>, 20  $\mu$ L well<sup>-1</sup> of media (for 2 mm media depth), 50  $\mu$ L well<sup>-1</sup> silicone oil (5 cSt) (for an additional 5 mm oil depth) overlay] were cultured for 12 h to reach a starting level of approximately 15% O<sub>2</sub> of POC. Two sets of mitochondrial stress compounds [carbonyl cyanide-4 (trifluoromethoxy) phenylhydrazine (FCCP, an uncoupling agent that maximizes the oxygen consumption of electron transport chain (ETC) Complex IV), and a mixture of rotenone (ROT, an inhibitor of ETC Complex I) and antimycin A (AA, an inhibitor of ETC Complex III)] were added to a culture well (0.4  $\mu$ L dose<sup>-1</sup>) in sequence to manipulate the mitochondrial respiration of the cells (Experimental Section). The pipette tip for compound delivery was pre-filled with oil to avoid introducing air to the media under oil during pipetting. Scale bar, 5 cm. d) Real-time (3 h) POC (the yellow-red line) of the reconditioning with regulated mitochondrial respiration. The oxygen sensor was placed on the cell layer without movement during the entire measurement process. The O<sub>2</sub> peak immediately after each compound loading was attributed to the dissolved oxygen in each dose (0.4  $\mu$ L) of the compound solution. The oxygen level of cell-free media at the test temperature ( $\approx 30$  °C, the blue line) was measured to be about 20% O<sub>2</sub>.

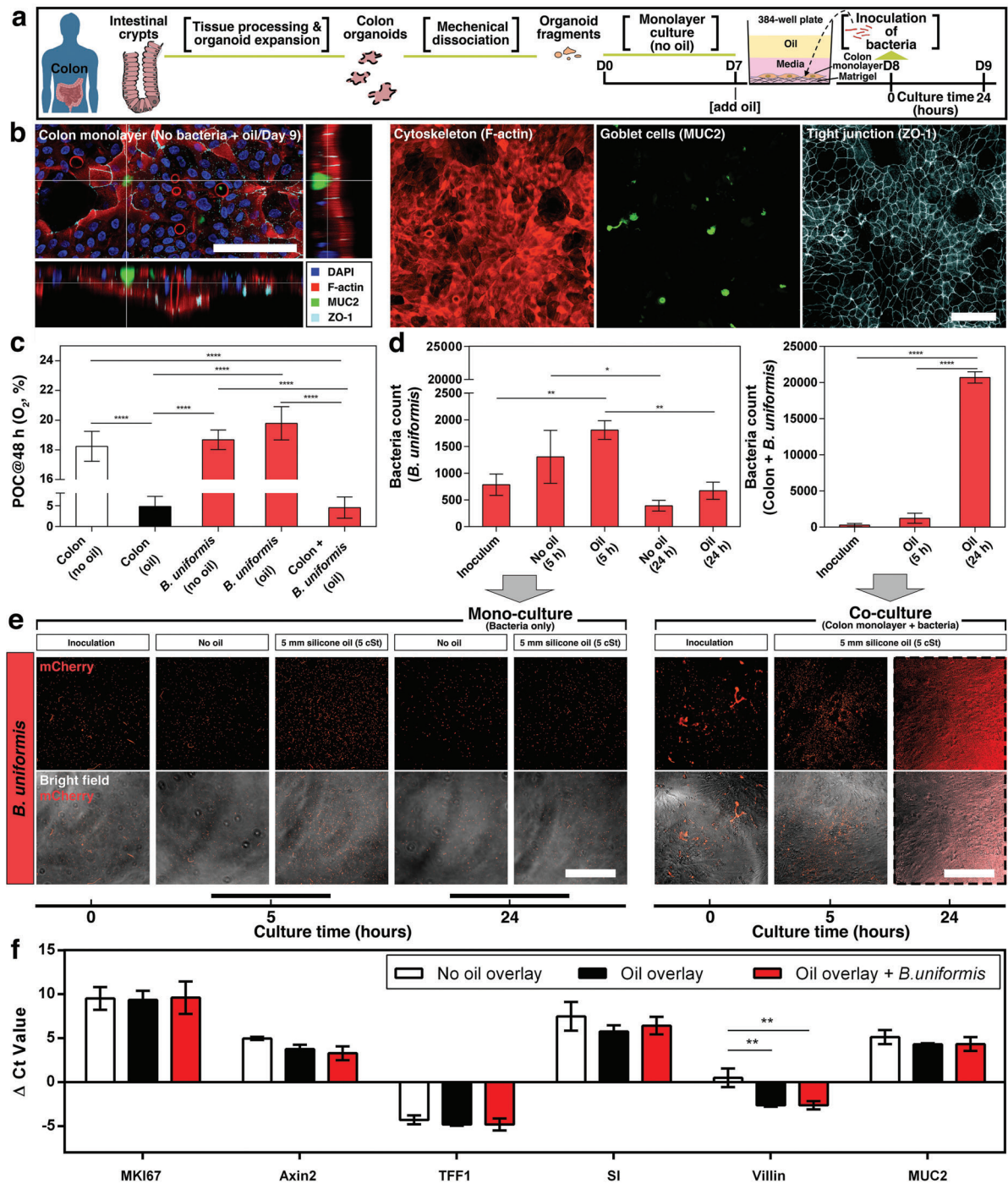


**Figure 6.** Under-oil coculture, cell function of primary colon epithelium, and growth kinetics of anaerobic bacteria (*B. uniformis*). a) Schematic showing the workflow of tissue processing, organoid generation, establishment of colon monolayer, and inoculation of bacteria. The volume of media is 40  $\mu\text{L}$  well<sup>-1</sup> for 4 mm in media depth. The volume of oil (silicone oil, 5 cSt) is 50  $\mu\text{L}$  well<sup>-1</sup> for 5 mm in oil depth. b) 3D laser confocal image with z-slices and fluorescent images from the under-oil monoculture of colon monolayer on Day 9. Scale bars, 100  $\mu\text{m}$ . c) POC ( $\text{O}_2$ , %) measured on Day 9 (i.e., at 48 h from adding the oil overlay) along with two no-bacteria monoculture conditions (i.e., colon monolayer only with and without oil overlay). Data were pooled and averaged with a minimum of 3 replicates of each condition. d) Bacteria count [at 30 $\times$  magnification, with a field of view of 446.5  $\mu\text{m}$  (length)  $\times$  445.6  $\mu\text{m}$  (width)] in (e). e) Microscopic images (30 $\times$  magnification) showing the growth in monoculture (bacteria only) with and without oil overlay compared to coculture (colon monolayer + bacteria) under oil. The fluorescent images were all processed with normalized LUTs for visualization. The 24 h *B. uniformis* images (in the dashed line box) were rendered with pseudocolor (red) to visualize the bacteria (Experimental Section). Scale bars, 200  $\mu\text{m}$ . f) RT-qPCR [ $\Delta\text{Ct}$  (i.e., cycle threshold)] results for comparison of gene expression (Table S2, Supporting Information) of the colon epithelium. Lower  $\Delta\text{Ct}$  values indicate higher gene expression. Data were pooled and averaged with 3 replicates of each condition. Error bars, mean  $\pm$  s.d. \* $p$   $\leq$  0.05, \*\* $p$   $\leq$  0.01, \*\*\* $p$   $\leq$  0.001, and \*\*\*\* $p$   $\leq$  0.0001.

lay, the oxygen levels were maintained close to atmospheric 21% O<sub>2</sub> over a 24 h period, indicating a negligible consumption of oxygen by *B. uniformis* [Figure 6c, *B. uniformis* (no oil/oil)]. Further substantiating this observation, the coculture of *B. uniformis* with colon monolayers yielded similar POC levels (2–8% O<sub>2</sub>) to colon cell monocultures indicating that oxygen consumption was dominated by colon epithelium.

We investigated the growth kinetics of *B. uniformis* in the monoculture and coculture conditions by quantifying the number of bacterial cells using fluorescent microscopy (Figure 6d,e). In bacterial monocultures, *B. uniformis* showed a moderate increase in abundance (Experimental Section) at an earlier time point of ≈5 h and then a decrease in abundance by 24 h. In contrast to the monoculture condition, *B. uniformis* exhibited reciprocal growth trends in the presence of colon monolayers in UOMS cell culture. Our results indicate that the growth of *B. uniformis* was significantly enhanced in the presence of the intestinal cells, leading to a dense and confluent layer blanketing the colon monolayer. One potential explanation for the observed growth enhancement is the reduced oxygen levels due to the metabolism of the intestinal epithelial cells under oil. Corroborating these trends, the oxygen microenvironments were substantially different in the monoculture and coculture conditions at 48 h based on the POC measurements [Figure 6c, *B. uniformis* (no oil/oil) vs colon + *B. uniformis* (oil)]. To further characterize the effect of oxygen on the growth of *B. uniformis* in the coculture, we performed a coculture experiment under fluorinated oil (Figure S13, Supporting Information). Compared to silicone oil, fluorinated oil has low moisture and high gas (e.g., O<sub>2</sub>, CO<sub>2</sub>) permeability (Figure 2a–f, Table 1). As shown in Figure S13 (Supporting Information), little hypoxia was generated from the coculture of the host cells (Caco-2) and the bacteria under fluorinated oil compared to cocultures under silicone oil. Importantly, no growth of *B. uniformis* was observed in the coculture performed under fluorinated oil in contrast to the growth observed in the coculture under silicone oil. While factors beyond oxygen may affect the growth of *B. uniformis*, the fluorinated oil control experiment suggests that elevated oxygen may contribute to the impaired growth of *B. uniformis* in this coculture relative to the silicone oil overlay.

The IFS analysis showed that expression of epithelial differentiation markers in colon monolayers were similar in presence and absence of *B. uniformis* (Figure S11, Supporting Information), suggesting that the presence of *B. uniformis* did not significantly disrupt the epithelium. To investigate the impact of *B. uniformis* and UOMS cell culture on colon monolayers at the transcriptional level, we examined the expression of gene markers associated with epithelial cell function, including cell proliferation (MKI67) and cell lineage (Axin2, TFF1, SI, and MUC2) (Table S2, Supporting Information). Our results showed that all investigated genes were robustly detected in all conditions (no oil overlay, oil overlay and *B. uniformis* coculture with oil overlay) by quantitative reverse transcription polymerase chain reaction (RT-qPCR) (Experimental Section). In addition, there were no significant changes in the expression of the proliferation marker gene (MKI67) and the majority of characteristic cell lineage markers associated with differentiation (Axin2, TFF1, SI, and MUC2) in response to UOMS cell culture (Figure 6f). Notably, the high abundance of *B. uniformis* did not significantly alter the differentiation status of the epithelium according to the subset of genes

examined, which is consistent with the IFS analysis results. However, our results indicate that the colon monolayer expression of villin, associated with brush border microvilli expressed by absorptive enterocytes, was upregulated in the conditions with UOMS cell culture compared to the control (i.e., no oil overlay) condition. Future studies are required to determine if the UOMS cell culture facilitates microvilli differentiation by upregulating the expression of villin and to confirm microvilli formation. Together, these results lend support to the hypothesis that the reduced oxygen level enabled by AROM in UOMS cell culture can establish a more favorable environment for the growth of strict anaerobes such as *B. uniformis*.

### 3. Conclusion

The critical role of oxygen in living systems is increasingly recognized; however, precise monitoring and control of oxygen levels are often neglected in cell culture studies. Many studies have highlighted the importance of mimicking in vivo physiological conditions (e.g., nutrients availability, temperature, pH and the partial pressure of vital gases such as O<sub>2</sub> and CO<sub>2</sub> of the cellular microenvironment) to improve modeling of specific cellular microenvironments in human physiology and disease. Nevertheless, employing a physiologically inconsistent oxygen microenvironment in cell culture is still a prevalent pitfall, which likely contributes substantially to differences between in vivo and in vitro results.<sup>[15]</sup> While the development of microscale cell culture enables precise control of the cellular microenvironment compared to standard cell culture at bulk scale, oxygen microenvironments that allow cellular control of the oxygen levels and achieve homeostasis (i.e., supply–demand balance) are lacking due to the material properties and small-scale nature of microscale technologies. In this work, we introduce AROM in UOMS cell culture, which provides a reliable approach capable of recapitulating a full range of oxygen levels via autonomous regulation by cells. Oxygen regulation by cells allows for establishment of feedback loops wherein the dynamically changing oxygen demands of cells modifies the oxygen microenvironment, which in turn triggers signaling pathways that affect cell functions and phenotypes. Using our method, the oxygen microenvironment is not imposed on the cells by the operator, and thus distinct from existing microscale cell culture methods (which primarily employ a supply-dominated or demand-dominated gas control on the cell culture system). With AROM, the cells are allowed to control oxygen autonomously via a supply–demand balance, which resembles the regulation of the oxygen microenvironment in vivo.

While this method aims to establish AROM in in vitro microscale cell culture, it could be applied to other vital gases (e.g., CO<sub>2</sub>) (Figure S14, Supporting Information). In microscale cell culture, especially PDMS-based microdevices, the dissolved gases in the culture media can change rapidly (due to the ultra-high gas permeability of PDMS elastomer and the small scale of the microdevice) if the ambient gas compositions change (e.g., moving the setup out of the incubator for intermediate sample manipulation or imaging). While this issue can be mitigated using a gas-regulating chamber equipped with a glove box and other tools (e.g., liquid handler, microscope), the complexity of such gas-regulating systems burdens the operation and discourages users from adopting those measures. UOMS cell culture mini-

mizes dependence on specifically defined ambient conditions for vital gas regulation. A culture or coculture can be established, maintained, and characterized directly in an atmospheric environment without using gas-regulating equipment.

To make the autonomous gas regulation complete as a scientific tool (i.e., being able to establish a specific microenvironment and perform quantitative measurements for tracking and investigating the process) the local level of such vital gases in the culture media to which the cells are exposed need to be effectively monitored. Compared to the culture systems with closed-channel or closed-chamber designs, UOMS cell culture allows minimal disturbance of the established cellular microenvironment by external interventions. As demonstrated in this work, a microsensor can be introduced through the oil overlay with spatiotemporal flexibility to monitor the local oxygen levels at time points and sites of interest. Similarly, cellular samples and/or reagents (e.g., drugs, conditioned media) can be easily added to or collected from UOMS cell culture without interfering with the gas levels in the cellular microenvironment. Moreover, by arranging different cell types and modulating the oil type, depth, or viscosity of the oil overlay, compartmentalization and high-throughput gas regulation and screening with different oxygen levels can be realized in a single device (e.g., a microtiter plate) against the same ambient environment such as in air or in a standard incubator. Temporarily changing oxygen levels seen in vivo such as fluctuating or cycling hypoxia can also be implemented by adding and removing a specific volume of oil in the oil overlay (e.g., with a programmed syringe pump) over time. The features enabled by the under-oil open design, could allow AROM to be used for high-throughput screening applications (e.g., mutant analysis of bacterial species or antimicrobial drug selection) with individually controlled oxygen microenvironments.

For in vitro microscale cell cultures that need to be maintained from several days to weeks, nutrients need to be replenished via media changes. To minimize interruption to the established oxygen microenvironment in UOMS cell culture during media change, we have demonstrated the use of partially deoxygenated media described in Figure S2 (Supporting Information). Deoxygenation of the culture media can be executed in several ways, including nitrogen gas ( $N_2$ ) bubbling, or a regular degassing/gas-exchange chamber. The deoxygenated media can subsequently be stored under oil and monitored using the oxygen sensor system as the oxygen level recovers to the target value (i.e., the oxygen level in an established microenvironment) required for media change.

Recently we reported a breakthrough in UOMS:<sup>[38]</sup> Enabled by the extreme wettability known as ELR,<sup>[23,25]</sup> open microchannels can be prepared under oil (silicone oil) with the channel dimensions reduced up to three orders of magnitude (from millimeter scale to micrometer scale) compared to previously reported techniques. Using this approach, open-fluid cell trapping (including mammalian cells and bacteria), range of flow rates comparable to blood flow, and anti-biofouling reversible open-channel fluidic valves can be achieved in open microfluidics. As demonstrated in these works, designer microchambers/microchannels and versatile fluidic control can be easily and robustly introduced to UOMS cell culture. Further, extension of the AROM method to under-oil open microchannels allows integration of flow conditions into the in vitro modeling.

We used the AROM method to investigate inter-kingdom interactions between primary human intestinal epithelium and a highly prevalent human gut microbiome species which exhibit contrasting responses to oxygen. Our results demonstrated that UOMS cell culture with AROM can be used to study the dynamics of inter-kingdom interactions at multiple levels, including bacterial growth, host-cell phenotypes, and gene expression. Future work will investigate the molecular basis of interactions using metabolomics, as well as study interactions using a diverse panel of human gut bacterial species and microbial communities constructed from the bottom up. In addition, future studies could investigate the genetic determinants of the bacterial growth dynamics in the presence and absence of host epithelium in AROM using barcoded transposon libraries<sup>[55]</sup> and/or deletions of key genes involved in oxygen sensing or tolerance.<sup>[54,56]</sup> Further, the ecological and molecular role of oxygen as a mediating factor in gut microbiome dysbiosis could be investigated using AROM. Specifically, shifts in microbial community composition, metabolite production and degradation, and host phenotypes could be quantified in response to oxygen perturbation to elucidate disease relevant host-microbiome interactions and feedbacks.<sup>[57]</sup>

The ability to control physical and chemical characteristics of cell culture in in vitro modeling enables improved function and relevance when recapitulating normal and disease states seen in vivo. The AROM in UOMS cell culture provides a simple Goldilocks principle-based approach for regulating vital gases and an improved capacity to mimic in vivo cellular microenvironments. The method can be robustly and readily integrated into existing in vitro microscale cell culture systems, allowing for broad adoption among end users.

## 4. Experimental Section

**COMSOL Multiphysics Simulation:** The simulation on COMSOL Multiphysics (Ver. 5.6) with the chemical reaction engineering (CRE) module (see the COMSOL Tutorial section in the Supporting Information) was performed. The temperature was set to 310.15 K and the pressure to 1 atm as the default model inputs. The models were established based on the geometry of a standard 384 well (Figure 1b). The boundary condition of the sidewalls was set to no flux. The partition condition boundary condition (a built-in function in the CRE module) defined different gas solubilities in neighboring materials (oil/media, etc.). Oxygen diffused from the top surface [21%  $O_2$  saturated (i.e., oxygen solubility) of a given material] (Table 1) to the bottom surface. The boundary condition at the bottom surface (i.e., the cell layer) accounted for the  $O_2$  demand =  $-(n \times OCR_{Avg} \times \rho_{cell} \times DF \times POC) / (Km0 \times S1 + POC)$ , where  $OCR_{Avg} = 2.5 \text{ amol cell}^{-1} \text{ s}^{-1}$  is the average OCR of human body cells,<sup>[58]</sup>  $n$  is the ratio between the OCR of a given cell type and  $OCR_{Avg}$ ,  $\rho_{cell}$  is cell density ( $3 \times 10^4 \text{ cells well}^{-1}$  as the default density that leads to near confluence in a standard 384 well from cell seeding of the typical mammalian cells),  $DF$  is a dimensionless cell density factor ranging from 0 to 1,  $POC$  is the oxygen concentration at the cell layer defined by COMSOL at a time,  $Km0$  is Michaelis–Menten constant of a given cell type (e.g., 5.6 mmHg for HUVEC), and  $S1$  is the solubility of oxygen in cell ( $1.049 \times 10^{-3} \text{ M atm}^{-1}$ ).<sup>[59]</sup> i) Influence of diffusion barrier on establishing an oxygen microenvironment (Figure 1b). In this section,  $n = 5$ ,  $DF = 1$  were used for the  $O_2$  demand. The diffusion barrier was set as PDMS elastomer, silicone oil (5 cSt), silicone oil (500 cSt) (Table 1) from left to right in Figure 1b, which gives hyperoxia, physioxia (i.e., about 5%  $O_2$  in homeostasis), hypoxia, and anoxia, respectively. ii) Reconditioning of an established oxygen microenvironment against the change from supply or demand (Figure 1d,e,g). The geometry of the models in this section was the same as the ones shown in Figure 1b. PDMS elastomer was

selected as the diffusion barrier material for the supply-dominated model (Figure 1d). For change from supply, the oxygen concentration was set at the top surface to:  $0.2 \times O_{2\_inMedia}$  ( $0.21 \text{ mol m}^{-3}$ ) from 0 to 8 h (Stage I),  $0.8 \times O_{2\_inMedia}$  from 8 to 16 h (Stage II), and  $0.7 \times O_{2\_inMedia}$  from 16 to 24 h (Stage III). Here  $n = 3.75$ ,  $DF = 1$  were used for the  $O_2$  demand. For change from demand, the surface reaction was set at the bottom surface to  $n = 4$ ,  $DF = 1$  from 0 h to 8 h (Stage I),  $n = 5$ ,  $DF = 1$  from 8 h to 16 h (Stage II), and  $n = 2$ ,  $DF = 1$  from 16 to 24 h (Stage III). Here  $O_{2\_inMedia}$  for the  $O_2$  supply was used. PS was selected as the diffusion barrier material for the demand-dominated model (Figure 1e). For change from supply, the oxygen concentration was set at the top surface to:  $1.0 \times O_{2\_inMedia}$  from 0 to 8 h (Stage I),  $0.9 \times O_{2\_inMedia}$  from 8 to 16 h (Stage II), and  $0.8 \times O_{2\_inMedia}$  from 16 to 24 h (Stage III). Here  $n = 0.5$ ,  $DF = 1$  were used for the  $O_2$  demand. For change from demand, the surface reaction was set at the bottom surface to  $n = 0.2$ ,  $DF = 1$  from 0 to 8 h (Stage I),  $n = 0.4$ ,  $DF = 1$  from 8 to 16 h (Stage II), and  $n = 0.8$ ,  $DF = 1$  from 16 to 24 h (Stage III). Here  $O_{2\_inMedia}$  was used for the  $O_2$  supply. Silicone oil (5 cSt) was selected as the diffusion barrier material for the supply–demand-balanced model (Figure 1g). For change from supply, the oxygen concentration was set at the top surface to:  $1.0 \times O_{2\_inMedia}$  from 0 to 8 h (Stage I),  $0.85 \times O_{2\_inMedia}$  from 8 to 16 h (Stage II), and  $0.95 \times O_{2\_inMedia}$  from 16 to 24 h (Stage III). Here  $n = 4$ ,  $DF = 1$  were used for the  $O_2$  demand. For change from demand, the surface reaction was set at the bottom surface to:  $n = 4$ ,  $DF = 1$  from 0 to 8 h (Stage I),  $n = 6$ ,  $DF = 1$  from 8 to 16 h (Stage II), and  $n = 2$ ,  $DF = 1$  from 16 to 24 h (Stage III). Here  $O_{2\_inMedia}$  was used for the  $O_2$  supply. iii) The kinetics of oxygen diffusion in multi-liquid-phase microsystems (Figure 2). In these models, the  $O_2$  demand was set at the bottom surface the same with  $n = 14$  and with  $DF = 1$  (for  $3 \times 10^4$  cells well $^{-1}$ ) or  $DF = 1/3$  (for  $1 \times 10^4$  cells well $^{-1}$ ) for different cell densities. The  $O_2$  supply was set at the top surface and the initial oxygen concentration in each layer based on the corresponding material (Table 1). The readout of oxygen level ( $O_2$ , %) was extracted from the cell layer at the bottom surface over 48 h. The .txt data sheets were exported and plotted in Prism Graphpad. The 3D diffusion profiles were generated in COMSOL with a color-coded  $O_2$ , % bar denoting 0% and 21%  $O_2$  in culture media. The figures were prepared in Adobe Illustrator.

**Measurement of POC and IOC:** i) Working principle of the optical oxygen sensor (for POC). The optical oxygen sensor system (Ohio Lumex) includes an oxygen meter [FireSting $O_2$  fiber-optical oxygen meter (PS FSO2-2)], a temperature sensor [Teflon-coated and submersible, not shielded,  $\varnothing = 2.1$  mm (PS TSUB21)], an oxygen mini sensor [ $\varnothing = 430$   $\mu\text{m}$  (OXB430)], and a computer installed with Firesting Logger software (Pyro Science). The measurement is based on quenching of near-infrared (NIR) fluorescence in the presence of molecular oxygen in the media. The quenching of fluorescence is described by Stern–Volmer relationship as  $I^0/I = 1 + K_{SV}[O_2]$ , where  $I^0$  and  $I$ , respectively, correspond to the fluorescence intensities in absence and presence of oxygen;  $K_{SV}$  is the Stern–Volmer constant, and  $[O_2]$  is the concentration of oxygen in the sample. ii) POC measurement with the optical oxygen sensor. The 384-well plate from cell culture was placed on a hot plate (40 °C, the set temperature) on the bench. An aluminum bar was applied between the well plate and the surface of the hot plate to enhance heat transfer. The temperature sensor was kept in a well (without cells) filled with 50  $\mu\text{L}$  DI water and with the tip sitting on the bottom of the well to give accurate temperature compensation. The system was allowed to stabilize for at least 5 min before the calibration, measurement, and data collection. Calibration of the optical oxygen sensor was done using the “2-point in water or humid air” mode with the steps as follows: #1) prepared the two calibration liquids. Liquid A—air-saturated DI water for 100%  $O_2$  saturation ratio (or 21%  $O_2$ ); Liquid B—freshly prepared 1 wt% sodium sulfite ( $\text{Na}_2\text{SO}_3$ ) ( $\geq 98\%$ , Sigma Aldrich, S0505) aqueous solution for 0%  $O_2$  saturation ratio (or 0%  $O_2$ ). Gave 5 min on Liquid B to reach the steady stage with 0%  $O_2$  before use. Added 50  $\mu\text{L}$  of each liquid to a well on the well plate and prewarm; #2) sterilized the oxygen sensor by submerging the sensor tip in 70% ethanol (Thermo Fisher Scientific, 64-17-5) in an Eppendorf tube for 10 s. Then thoroughly rinsed the sensor tip with DI water and dried it in air using a rubber bulb; #3) kept the oxygen sensor in Liquid A first until the oxygen

readout curve was stabilized at 100%  $O_2$  saturation ratio (with minimal background fluctuation). Then switched to Liquid B to have the oxygen readout curve stabilized at 0%  $O_2$  saturation ratio. Thoroughly rinsed the sensor tip with DI water and dried it in air using the rubber bulb; #4) inserted the oxygen sensor mounted on a linear translation stage (Siskiyou, MX130L) into a well through the oil overlay with the sensor tip resting on the cell layer at the bottom of the well to give an accurate readout of POC. Each recording of the POC lasted an equal length of time (e.g., 1 min) after the reading is stable. The replicate wells from the same cell type and condition were measured in a row without additional treatment of the sensor tip during switch. To switch to a different cell type or condition, the sensor tip was sterilized following Step #2 before the next measurement to avoid cross contamination; #5) after all measurements finished, cleaned the oxygen sensor following Step #2; 6) the recorded .txt data sheets ( $O_2$  % vs time) were pooled together for each condition in Excel and then plotted in Prism GraphPad. iii) Working principle of the hypoxia dye (for IOC). The measuring of the hypoxia dye is based on the uptake of the dye molecules into live cells that fluoresce when experiencing a reduced oxygen level inside the cells (i.e., IOC) compared to 21%  $O_2$ . Dead cells release the dye and lose fluorescence. Several pitfalls from using this hypoxia dye need to be clarified: #1) The dye only provides a fluorescence readout that can be used to reflect/track the drop of IOC compared to 21%  $O_2$ . The fluorescence intensity from a single condition on itself is not sufficient to indicate any specific oxygen levels unless benchmarked to a direct oxygen level readout, e.g., POC measured at the cell layer (which is the protocol used in this work); #2) moreover, the fluorescence intensity varies with different operation parameters including the concentration of the dye in media and imaging conditions (e.g., the bottom material/thickness of the well plate, laser intensity, exposure time). A parallel comparison of the fluorescence intensity is valid only if the operation parameters are defined and maintained consistent; #3) at last, the brand name of the dye (Hypoxia Reagent) itself is apparently based on the conventional definition of “normoxia” with 21%  $O_2$ , however, inaccurate and misleading.<sup>[60]</sup> An increased fluorescence compared to the baseline with 21%  $O_2$  might indicate an oxygen level anywhere between hyperoxia and anoxia (Figure 1a,b). Therefore, the hypoxia dye does not only report hypoxia. iv) IOC tracked by the mean fluorescence intensity of the hypoxia dye. Fluorescent imaging was performed on a Nikon Ti Eclipse inverted epifluorescence microscope (Nikon Instruments) with 3 replicate wells from each condition to get the hypoxia dye signal at  $4 \times$  magnification (to cover the cell layer from the whole well on a 384-well plate) with 485 nm/525 nm [Excitation (Ex)/Emission (Em)], maximum laser power, and 1 s of exposure time. Wells with the same cell seeding but without hypoxia dye were imaged for control and background subtraction during image processing and analysis of the mean fluorescence intensity. The mean fluorescence intensity was extracted from an image (in 16-bit color depth, with and without hypoxia dye) using the “Analyze → Measure” function in Fiji ImageJ, with a range of interest (ROI) set to cover the cell layer but exclude the edges of a well. The mean fluorescence intensities of images with hypoxia dye were subtracted with the average of the mean fluorescence intensities from the control without hypoxia dye.

**Oxygen Diffusion Test of Silicone Oil:** 1 mL of culture media (DMEM + 10% FBS) was pipetted to a 5 mL centrifuge tube (polypropylene, Argos, T2076A). The oxygen sensor was submerged in the media with the tip kept at about 1 mm from the air/media interface (Figure S2, Supporting Information). A stainless-steel blunt needle (18G, SAI Infusion Technologies, B18-150) was connected to a  $N_2$  cylinder via a silicone tubing (Tygon) and then kept close to the bottom of the centrifuge tube to perform  $N_2$  bubbling. The  $N_2$  flow rate was set at about  $4 \text{ mL min}^{-1}$ .  $N_2$  bubbling was let run for about 500 s ( $\approx 8$  min) to reach 0%  $O_2$  of the media.  $N_2$  bubbles got accumulated at the air/media interface and were removed by keeping the needle in the bubble layer for a few seconds. After the  $N_2$  bubbles were removed the  $N_2$  gas trapped in the centrifuge tube was purged by a rubber bulb for 3 times to create the air (i.e., no oil) condition or was directly replaced by silicone oil (3 mL) [Sigma Aldrich, 317667 (5 cSt), 378399 (1000 cSt)] added by pipette. The 3 mL of oil added on top of the media in the 5 mL centrifuge tube led to about 18 mm in the oil depth. Then the oxygen recovery was recorded with the optical oxygen sensor until the oxygen level

reached about 10% O<sub>2</sub>. The recorded .txt data sheets (O<sub>2</sub> % vs time) were plotted in Excel.

**UPLC-MS Media Analysis:** The objective of this assay is to compare silicone oil and fluorinated oil treated media to control media for relative quantification of media composition change. The equipment is a tandem of a liquid chromatography (LC) system (Dionex UPLC) with Amino Acid columns (Kinetix Imtakt Intrada mixed mode Amino Acid, 3 × 150 mm) and a Mass Spectrometer [Thermo Q-Exactive (QE) Orbitrap]. Samples include control media (DMEM + 10% FBS + 1% Pen-Strep), silicone oil (5 cSt), and fluorinated oil (Fluorinert FC-40) (Sigma Aldrich, F9755) treated media (Figure 3a) for 3 independent replicates of each condition. Samples were prepared with the steps as follows: #1) added 300 μL precipitation mix (acetonitrile with formic acid and *d*<sub>6</sub>-GABA internal standard) to 9 Sirocco wells; #2) added 100 μL each sample to each well and let sit for 2 min; #3) pushed through the plate, dry under nitrogen, and resuspend dried samples in 100 μL 0.1% formic acid/water for amino acid runs; #4) injected 2 μL of each sample in duplicate on QE using a top 5 ms ms<sup>-1</sup> method with a scan range of 80–700 *m/z*. Also made 1 pooled quality control sample of equal molar concentration of all 9 samples (injected twice) for normalizing data during data analysis. Method run on UPLC amino acid—Solvent A (acetonitrile/0.3% formic acid); Solvent B (water 100 × 10<sup>-3</sup> M ammonium formate); Flow (0.5 mL min<sup>-1</sup>); Column Temp (60 °C); Max Pressure Limit (7000 psi); Running pressure (1000 psi). Method run on QE – FULL MS/DD-MS. (TOPN) – Full MS: microscans (1); resolution (70000); automatic gain control (AGC) target (1e6); maximum injection time (IT) (100 ms); scan range (80–700 *m/z*); spectrum data type (Profile). Microscans 1: resolution (17500); AGC target (1e5); maximum IT (100 ms); loop count (5); Isolation window (3.5 *m/z*); normalized collision energy (NCE) (30.0); spectrum data type (Centroid); peptide match (off); exclude isotopes (on); dynamic exclusion (1.0 s). The following filters were used when analyzing the data using Compound Discoverer 3.0 (Thermo Scientific Metabolomics Software): #1) base peak intensity of all samples > 1e5. This filter was for picking peaks that were above background noise level; #2) masses for identified compounds had to be within 5 ppm of theoretical values; #3) ms ms<sup>-1</sup> patterns of identified compounds had to match theoretical fragmentation patterns; #4) percent coefficient of variations (CVs) for replicates within a given condition or control had to be <20%; #5) data was normalized using the 2 injections of the pooled quality control sample (Median Absolute Deviation). Meta data from Compound Discoverer 3.0 (filtered data only): #1) a total of 193 peaks (compounds) were aligned between the control and treated samples and passed all above filters; #2) of the 193 compounds, 39 were identified using molecular weight and ms ms<sup>-1</sup> fragment patterns using above filters; #3) for the silicone oil samples none of the identified compounds showed any difference in regulation in comparison with the control media samples. However, two of the unidentified compounds had adjusted *p*-values that were significant when compared to the control; #4) similarly, for the Fluorinert FC-40 samples none of the identified compounds showed any difference in regulation in comparison with the control samples. Additionally, two unidentified compounds [different mass and retention time (RT) than for the silicone oil] had adjusted *p*-values that were significant when compared to the control; #5) an Excel report that has all the relevant information (relative intensity, compounds masses, names, statistics) was generated using the filtered data; #6) the HLB values of the identified molecules were obtained in Chemicalize (ChemAxon). The AUCs (i.e., area under the curve) of the top five lipophilic molecules with HLB ranging from 0 to about 6 were plotted in Prism GraphPad.

**Preparation of Monoculture Plates:** The monoculture was established in (but not limited to) 384-well plates (Polystyrene, Tissue Culture Treated, Flat Bottom, 384-well plate, Corning 3701) with cell culture media corresponding to each cell type (Table S1, Supporting Information), and with silicone oil or fluorinated oil (Fluorinert FC-40) overlay. The culture media and oil in this work were not deoxygenated prior to use. The plates were prepared in a sterile biosafety hood in air at room temperature (RT, ≈22 °C). Specifically, to prepare a monoculture plate include the following steps: #1) added a certain volume (e.g., 15 or 35 μL well<sup>-1</sup>) of fresh media (stored in a regular 4 °C fridge, oxygen saturated) with and without the hypoxia dye (Invitrogen, Image-iT Green Hypoxia Reagent, Thermo Fisher

Scientific, 114833) (1:1000 dilution in media); #2) overlaid the media with a certain volume [e.g., 0 (for no-oil control), 10 or 50 μL well<sup>-1</sup>] of oil; it is worth noting that the density of Fluorinert FC-40 (1.85 g mL<sup>-1</sup>) is much larger than culture media (0.998–1 g mL<sup>-1</sup>) and those nonfluorinated liquids (e.g., about 0.97 g mL<sup>-1</sup> for silicone oil). 15 μL or less of the volume of FC-40 could be held stably on top of the media layer in a standard 384 well. Either a larger well (e.g., 96-well plates) or larger volume (i.e., > 15–20 μL) of FC-40 was used, the fluorinated oil was settled down and pushed the culture media to the top layer. If a larger container or volume of fluorinated oil is required, surface chemistry could be introduced contrast to stabilize the oil–oil or oil–media interface.<sup>[23,25,38]</sup> #3) prewarmed the plate in a standard incubator [37 °C, 18.6% O<sub>2</sub>, 5% CO<sub>2</sub>, 95% RH] before cell seeding; #4) prepared the cell stock at a specific concentration (e.g., 2000 or 6000 cells μL<sup>-1</sup>) following the standard cell culture/passage protocol; #5) pipetted 5 μL of the cell stock to the media under oil to reach a target seeding density (e.g., 1 × 10<sup>4</sup> or 3 × 10<sup>4</sup> cells well<sup>-1</sup>); #6) kept the plate in a standard incubator up to 24 or 48 h without media change. The plates were imaged and measured to get different readouts, e.g., cell viability, POC and IOC (see details in measurement of POC and IOC above).

**Preprocessing of Cells in Monoculture:** i) Preculture of *C. albicans*. *C. albicans* fungal cells (CMM16) were inoculated from a streaked plate in 2 mL yeast extract peptone dextrose (YPD) [1% yeast extract (BD Biosciences, 212730), 2% peptone (BD Biosciences, 211862), 2% dextrose glucose (Thermo Fisher Scientific, 215510)] glucose media, and grown in an incubator at 30 °C overnight. The fungal cells were measured on a spectrophotometer (Thermo Fisher Scientific, 335932) with optical density at a wavelength of 600 nm (OD<sub>600</sub>) and then converted to cell concentration. Serial dilution was performed to reach a final concentration of 6000 cells μL<sup>-1</sup> in a culture media (Table S1, Supporting Information) for further experiments. ii) Isolation of neutrophils from whole blood. Primary human neutrophils were isolated from peripheral blood taken from healthy donors. All blood samples were drawn according to Institutional Review Boards (IRB)-approved protocols per Declaration of Helsinki at the University of Wisconsin-Madison. Peripheral neutrophils were isolated by negatively removing all contaminating cells using the MACSxpert Neutrophil Isolation Kit (Miltenyi Biotec, 130-104-434) and BD Pharm Lyse buffer (BD Biosciences, 555899) for red blood cell depletion, according to manufacturer's instructions. Cells were washed and resuspended in appropriate media (Table S1, Supporting Information) for further experiments.

**Preparation of Monoculture in PDMS Microchannels:** The PDMS microchannels (about 2500 μm in length, 600 μm in width, and 250 μm in height) (Figure S3, Supporting Information) were prepared following a standard photolithography process and O<sub>2</sub> plasma bound onto a chambered coverglass [Nunc Lab-Tek II Chambered Coverglass, #1.5 borosilicate coverglass (0.16–0.19 mm), biocompatible acrylic adhesive, Thermo Fisher Scientific, 155382]. Collagen type I (Corning, 354249) solution prepared with 10 × phosphate-buffered saline (PBS), cell culture media, and 0.5 M NaOH at 3 mg mL<sup>-1</sup> was added to the glass surface in the microchannels to create a thin layer of collagen coating prior to polymerization. After polymerization of the collagen coating at 37 °C, 30 μL of Caco-2 cells at a concentration of 15000 cells μL<sup>-1</sup> in culture media (EMEM + 20% FBS) were seeded into each microchannel via passive pumping and cultured for 24 h. After 24 h cell culture the conditioned media (along with the suspension cells) was replaced with a fresh media containing hypoxia dye. The microchannels were then overlaid with a 2.5 mm depth of fluorinated oil (Fluorinert FC-40), followed by an additional 5 mm depth of silicone oil (1000 cSt). The chambered coverglass with the PDMS microchannels was kept in a standard incubator for 48 h without media change before the characterization and imaging on a microscope (see IOC tracked by the mean fluorescence intensity of the hypoxia dye).

**Reconditioning of the Under-Oil Oxygen Microenvironment:** This test was performed by regulating mitochondrial respiration in UOMS cell culture. A 384-well plate of Caco-2 cells was prepared (see preparation of monoculture plates) by seeding 1 × 10<sup>4</sup> cells well<sup>-1</sup> in 20 μL of culture media (EMEM + 20% FBS) with 5 mm silicone oil (5 cSt) overlay. The cells were cultured for 12 h to reach a starting level of POC at about 15% O<sub>2</sub>. A mitochondrial stress assay kit (Agilent Technologies, Seahorse XFp, 103010–100) was used to manipulate the mitochondrial respiration

and thus the OCR of the cells. Specifically, FCCP [carbonyl cyanide-4 (trifluoromethoxy) phenylhydrazone] collapsed the proton gradient and disrupted the mitochondrial membrane potential. As a result, electron flowed through the ETC (i.e., Electron Transport Chain) was uninhibited, and oxygen consumption by Complex IV reached the maximum. A mixture of ROT (rotenone)/AA (antimycin A) inhibited Complex I and Complex III. This combination shut down mitochondrial respiration. FCCP and the mixture of ROT/AA were reconstituted in DMEM culture media (not deoxygenated) to get a  $50 \times 10^{-6}$  and  $25 \times 10^{-6}$  M compound solution, respectively. The POC was monitored in real time for 3 h by the optical oxygen sensor (see POC measurement with the optical oxygen sensor) with the culture plate set on a hot plate. The compound solutions were added to a well at a volume of  $0.4 \mu\text{L dose}^{-1}$  [for a 1:50 v/v ratio ( $0.4 \mu\text{L}$  compound solution:20  $\mu\text{L}$  media)] in a sequence (4 doses of FCCP and 2 doses of ROT/AA). To avoid introduction of air during the pipetting under oil, the pipet tip was pre-filled with oil and then loaded with  $0.4 \mu\text{L}$  of the compound solution. Compounds were added to the culture media with the pre-filled oil kept in the tip.

**Colorimetric Analysis of pH in Cell Culture With and Without Oil Overlay:** The test was performed with monoculture of Caco-2 cells (see preparation of monoculture plates) compared to a no-cell control (Figure S14, Supporting Information). The culture media (EMEM + 20% FBS) was supplemented with a pH indicator (phenol red,  $30 \times 10^{-6}$  M). A pH color chart was obtained using a pH meter (Model 225, Electrode Model 300731.1, Denver Instrument) and hydrochloric acid (1 M) titration. 10 mL of the media was added to a 50 mL centrifuge tube (Falcon, 734-0451). Hydrochloric acid was added to the media to reach a specific pH reading. 20  $\mu\text{L}$  of the pH-adjusted media was pipetted to a well of a 384-well plate and then pictured (iPhone 6s) against a white background. For the culture and control plates, each condition has at least 3 replicates. The plates were pictured before and 24 h after incubation in a standard incubator with different exposure times (i.e., 0, 30, and 100 min) in air at room temperature. The color of the media in comparison with the pH color chart indicates the pH level of the media in a tested condition, reflecting a reduced  $\text{CO}_2$  diffusion from media to ambient ( $\approx 0.04\%$   $\text{CO}_2$ ) with the oil overlay.

**Live–Dead Staining and Cell Viability Analysis:** Cells were stained with  $2 \times 10^{-6}$  M calcein AM (Thermo Fisher Scientific, L3224),  $1 \times 10^{-6}$  M propidium iodide (Thermo Fisher Scientific, P1304MP), and Hoechst 33342 (Thermo Fisher Scientific, H3570) in appropriate culture media (Table S1, Supporting Information), following 24 h of culture to obtain live, dead, and nuclei counts, respectively. Staining solution was prepared at  $2 \times$  immediately before staining and diluted in culture media within wells to make  $1 \times$  solution. Cells were incubated with staining solution for 20 min in a standard incubator prior to imaging. Fluorescent images were obtained on a Nikon Ti microscope and kept at  $37^\circ\text{C}$  and 5%  $\text{CO}_2$  via an on-stage incubator (Bold Line, Okolab) during imaging. A minimum of 3 replicate wells with live cells were averaged for viability analysis. The dead-channel images were threshold processed using the “Image  $\rightarrow$  Adjust  $\rightarrow$  Threshold (Default)” function in Fiji ImageJ. Threshold adjustment was carried out on the entire image including the edges of the well. Minimal adjustment might be applied manually if necessary to get the optimal threshold-processed images that loyally distinguish and pick the cells. With the seeding densities in this study (i.e.,  $1 \times 10^4$  or  $3 \times 10^4$  cells  $\text{well}^{-1}$  of a 384-well plate), cell clumping could happen. The cells in a clump could not be effectively identified by the software as separate entities, which caused negative errors on cell count. The binary watershed function “Process  $\rightarrow$  Binary  $\rightarrow$  Watershed” in Fiji ImageJ was chosen to process the image further so that the clumps were broken into smaller particles to give a more accurate cell count of the true number of cells by the software. On the processed images, particle analysis was carried out using the “Analyze  $\rightarrow$  Analyze Particles...” function in Fiji ImageJ, which gave the cell count (of the dead cells in this case) in the output. In theory, the total cell count (including both live and dead cells) could be obtained by analyzing the nuclei-channel images. However, cell clumping became a dominant effect on the nuclei-channel images, which led to a severely underestimated number of the total cell count. Provided such a limit, the total number of cells was used in each seeding density (i.e.,  $1 \times 10^4$  or  $3 \times 10^4$  cells  $\text{well}^{-1}$ ) instead to calculate

the cell viability, following the equation: cell viability = live cells/total cells  $\times 100\%$  = (total cells – dead cells)/total cells  $\times 100\%$ .

**Preparation of Coculture Plates:** The coculture was performed in 384-well plates [Glass Bottom (#1.5,  $0.170 \pm 0.005$  mm, high performance coverglass), Black polystyrene frame, Tissue Culture Treated, Flat Bottom, 384-well plate, Cellvis, P384-1.5H-N] with the steps as follows: i) isolation of intestinal crypts and generation of colon organoids. All human studies were approved by an IRB at University of Wisconsin-Madison (Protocol# 2016-0934). Intestinal crypts were isolated from colon removed for nonmalignant etiology using a previously established protocol.<sup>[61]</sup> Isolated crypts were embedded in Matrigel (Basement membrane, Corning, 354248), and cultured in 24-well plates (Polystyrene, Nunc, Non-Treated Multidishes, Thermo Fisher Scientific, 144530) in intestinal stem cell media (Table S1, Supporting Information). Colon organoids were split 1:2 to 1:4 every 2 to 3 days using a previously established protocol.<sup>[62]</sup> ii) Culture of colon monolayer. Based on the established protocol,<sup>[62]</sup> intestinal stem cell media was removed from the 24-well plates containing colon organoid cultures, 500  $\mu\text{L}$  of  $0.5 \times 10^{-6}$  M ethylenediaminetetraacetic acid (EDTA) in PBS was added to each well and Matrigel plugs containing the organoids were harvested. After centrifugation at room temperature for 3 min at  $300 \times g$ , supernatant was removed. 1 mL of  $2.5 \text{ mg mL}^{-1}$  trypsin (Sigma Aldrich, T4549) was added and incubated for 2 min in a  $37^\circ\text{C}$  water bath. Trypsin was neutralized using media [Advanced DMEM/F12, Thermo Fisher Scientific, 12634-010] + 20% FBS. The organoids were broken down into small fragments by pipetting vigorously using filtered 1000  $\mu\text{L}$  pipette 60 times. 20000 organoid fragments ( $500$  fragments  $\mu\text{L}^{-1}$ ) were seeded onto a 384-well plate coated with Matrigel that was diluted 1:40 in intestinal stem cell media. Media was changed every 2 to 3 days (stem cell media). After 7 days, a confluent monolayer was formed, and the media was switched to  $40 \mu\text{L well}^{-1}$  of differentiation media (for 4 mm in media depth) (Table S1, Supporting Information) and  $50 \mu\text{L well}^{-1}$  of oil (silicone oil, 5 cSt) (for 5 mm in oil depth) was overlaid. Bacterial cocultures were performed on the following day. iii) Preculture and fluorescent tagging of gut anaerobic bacteria. *B. uniformis* (DSM 6597) was cultured in an anaerobic chamber (Coy Labs) with 83%  $\text{N}_2$ , 2% hydrogen ( $\text{H}_2$ ) and 15%  $\text{CO}_2$  at  $37^\circ\text{C}$  in Anaerobic Basal Broth (ABB, Oxoid) for all steps except conjugation. During the conjugation procedure, *B. uniformis* was cultured in Brain Heart Infusion Broth (BHIS, Sigma Aldrich). The conjugation donor *E. coli* strain BW29427 was obtained from the *E. coli* Genetic Stock Center (CGSC). This strain was grown aerobically in Luria Bertoni (LB, Sigma Aldrich) media containing  $25 \times 10^{-6}$  M of 2,6-diaminopimelic acid (DAP, Sigma Aldrich). The *E. coli* strain BW29427 was transformed with the plasmid pWW3515 that harbored the fluorescent reporter mCherry expressed from the BfP1E6 promoter.<sup>[63]</sup> The pWW3515 plasmid encoded the IntN2 tyrosine integrase, which mediated recombination between the *attN* site on the plasmid and one of the two *attBT* sites on the *B. uniformis* chromosome.<sup>[64–67]</sup> Following the transformation, single colonies were inoculated into LB containing  $100 \mu\text{g mL}^{-1}$  carbenicillin (Carb, IBI Scientific) and DAP and incubated at  $30^\circ\text{C}$  overnight. Cell pellets were collected by centrifugation at 4000 rpm for 5 min and washed with fresh LB media. The *E. coli* cells were then combined with the *B. uniformis* culture ( $\text{OD}_{600} = 0.5–0.6$ ) at a donor:recipient ratio (v/v) of 1:10. The cell mixture was pelleted, resuspended in 0.2 mL BHIS and then spotted on BHISAD (BHIS + 10% ABB + DAP) agar plates and incubated anaerobically at  $37^\circ\text{C}$  for 24 h. The cell lawns were scraped and resuspended in BHIS and plated as serial dilutions on BHISAGE plates [BHIS supplemented with 10% ABB,  $200 \mu\text{g mL}^{-1}$  gentamicin (Sigma Aldrich) and  $25 \mu\text{g mL}^{-1}$  erythromycin (Sigma Aldrich)] and incubated anaerobically at  $37^\circ\text{C}$  for 2 days. The engineered strain was verified by colony PCR. Bacterial inoculum onto the 384-well plate was captured in exponential phase, diluted to an  $\text{OD}_{600}$  of 0.1 in the culture media (e.g., the differentiation media for primary colon epithelium). iv) coculture of colon monolayer with gut anaerobic bacteria. The bacterial inoculum stock ( $\text{OD}_{600} = 0.1$ ) was prepared in the anaerobic chamber and transported in an anaerobic Hungate tube (VWR, 100484-346). The following inoculation was performed in air in a sterile biosafety hood. An Eppendorf tube (Polystyrene, 0.6 mL) was pre-filled with 300  $\mu\text{L}$  of silicone oil (5 cSt). 100  $\mu\text{L}$  of the bacterial inoculum was transferred from a Hungate tube to under oil in the Eppendorf



tube using a syringe (1 mL, Luer-lok Tip, BD Biosciences, REF 309628). Bacteria were added to the media above the colon monolayer by pipette at 1:20 v/v ratio (2  $\mu$ L bacteria:40  $\mu$ L media) carefully so as not to disrupt the oil overlay. Monoculture conditions (including bacteria only and colon monolayer only) with and without oil overlay were prepared in parallel as control. Following the inoculation, the culture plates were kept in a standard incubator and cultured for 24 h.

**Downstream Characterizations in Coculture:** i) RT-qPCR (colon monolayer). After 24 h of coculture, the overlaying oil and media were carefully removed, and each well was washed with Dulbecco's PBS (Thermo Fisher Scientific, 14190250). To each well, 20  $\mu$ L of Buffer RLT plus +  $\beta$ -mercaptoethanol (Sigma Aldrich, M3148) was added to lyse the cells. RNA was isolated using Qiagen RNeasy Plus Micro Kit (Qiagen, 74034) according to the manufacturer's protocol and quantified with a pico chip on an Agilent Bioanalyzer (Santa Clara, CA). Reverse transcription was conducted with the RNA to cDNA kit (4387406, ThermoFisher Scientific). A preamplification step that amplified the amount of cDNA available for downstream RT-qPCR analysis was conducted using SsoAdvanced PreAmp Kit (BioRad, 1725160). RT-qPCR was performed using TaqMan Gene expression assays (Thermo Fisher Scientific) with LightCycler 480 Probes Master (Roche Diagnostics). A 20  $\mu$ L total reaction volume was used with 1  $\mu$ L of 20  $\times$  TaqMan primer-probe mix, 10  $\mu$ L of 2  $\times$  LightCycler 480 Probes Master mix, and 9  $\mu$ L of cDNA diluted in RNase-free water. RT-qPCR amplification was monitored using a LightCycler 480 (Roche Diagnostics). qPCR was performed on 8 target genes and 3 reference genes (Table S2, Supporting Information). The reference genes were selected based on constitutive and stable expression across sample types. After incubation at 95  $^{\circ}$ C for 10 min, the reactions underwent 45 cycles as follows: 10 s at 95  $^{\circ}$ C, 30 s at 60  $^{\circ}$ C, and 1 s at 72  $^{\circ}$ C. Genes with Ct  $\geq$  35 were excluded. The Ct values were normalized to the reference genes (GAPDH, HPRT and RPLP0). Quantification of results (Figure 6f) are presented as:  $\Delta$ Ct = [CtGene - mean(CtGAPDH, CtHPRT, CtRPLP0)] so that positive values represent low expression and negative values represent high expression compared to the reference genes. ii) Immunostaining (colon monolayer). The cells on a 384-well plate were fixed first by adding 40  $\mu$ L of 4% paraformaldehyde (PFA) to each well and then incubated at room temperature for 10 min. After the PFA solution was removed by pipette, the fixed cell layer was washed with 100  $\mu$ L of 1  $\times$  PBS for three times. After fixation, the cells were permeabilized by adding 40  $\mu$ L of 0.1% Triton X-100 to each well and then incubated at room temperature for 5 min. After the Triton solution was removed by pipette, the permeabilized cell layer was washed with 100  $\mu$ L of 1  $\times$  PBS for three times. After permeabilization, a blocking buffer consisting of 3% bovine serum albumin (BSA), 5% human serum, and 0.1 M glycine in 0.1% PBST (1  $\times$  PBS with 0.1% added Tween 20) was added to each well at a volume of 80  $\mu$ L. The plate was stored in a cold room overnight at 5  $^{\circ}$ C to prohibit nonspecific binding of antibodies in the following staining process. Before staining, the blocking buffer was removed by pipette and the wells were washed with 100  $\mu$ L of 1  $\times$  PBS three times. A staining buffer was prepared utilizing 3% BSA in 0.1% PBST and 10% of a 1% Tween 20 solution at a 1:25 or 1:50 concentration with a primary antibody [(DAPI, 1:2500 dilution, Thermo Fisher Scientific, D3571), (F-actin, 1:500 dilution, Thermo Fisher Scientific, T7471), (Rabbit polyclonal anti-FABP1, 1:25 dilution, Sigma Aldrich, HPA028275), (Mouse monoclonal anti-MUC2, 1:50 dilution, Santa Cruz Biotechnology, sc-515032), (Villin, Novus Biologicals, NBP2-53201), (Rabbit polyclonal anti-ZO-1, 1:25 dilution, Thermo Fisher Scientific, 61-7300), and (Mouse monoclonal anti-E-cadherin, 1:25 dilution, BD Biosciences, 610182)]. The staining buffer and accompanying antibody were added at a volume that was just large enough to cover the cell layer at the bottom of each well ( $\approx$ 10  $\mu$ L). The plate was stored in a cold room overnight at 5  $^{\circ}$ C. Removal of the buffer was followed by two washes of 0.1% PBST of about 100  $\mu$ L well $^{-1}$ . A secondary antibody [488-anti-mouse, 1:250 dilution, Abcam, ab150105] or [647-anti-rabbit, 1:250 dilution, Abcam, ab150075] depending on the compatibility of the original primary antibody was mixed with the staining buffer at 1:250 concentrations along with a 1:5000 concentration (sometimes 1:3000 depending on available product) of DAPI to stain the nuclei and a 1:500 concentration of rhodamine phalloidin to stain the (F-actin) cytoskeleton. This final staining solution was added to

each well at a volume of 10  $\mu$ L well $^{-1}$  and then the plate was incubated for 1 h at room temperature while protected from light using aluminium foil. Following the incubation, the wells were washed with 0.1% PBST for two times before imaging. iii) Fluorescent/confocal microscopy. The fluorescent images and videos were taken on a Nikon Ti Eclipse at 4  $\times$ , 15  $\times$  (10  $\times$  objective with the 1.5  $\times$  tube lens), and 30  $\times$  (20  $\times$  objective with 1.5  $\times$  tube lens) magnifications with bright field and fluorescent channels, including 390 nm/440 nm [Excitation (Ex)/Emission (Em)] for nuclei (DAPI); 485 nm/525 nm for hypoxia dye (Image-iT Green Hypoxia Reagent), live dye (calcein AM), goblet cells (MUC2), microvilli (Villin); 560 nm/607 nm (Ex/Em) for dead dye (propidium iodide), mCherry, and cytoskeleton (F-actin); and 648 nm/684 nm for tight junction (ZO-1). Maximum laser power was applied if not stated otherwise. 3D confocal images were acquired with a Nikon A1-Si laser-scanning confocal microscope (Nikon Instruments). iv) Bacteria count. The 30  $\times$  magnification fluorescent images were threshold processed using the "Image  $\rightarrow$  Adjust  $\rightarrow$  Threshold (Triangle)" function in Fiji ImageJ. And then the bacterial cells were picked up and counted using the "Process  $\rightarrow$  Find Maxima..." function in Fiji ImageJ. A prominence threshold was applied to each image to reach an optimal pickup of the signal (i.e., cells) against the noise (i.e., background). The bacteria count results were averaged with a minimum of 3 replicates of each condition and plotted in Prism GraphPad. Note that *B. uniformis* stably express the mCherry proteins at low density (e.g., at early time points after inoculation). However, at 24 h, *B. uniformis* grew into a highly dense layer in coculture, mostly losing their fluorescence due to the repressed expression of mCherry in low oxygen levels. The bacteria showed up in the bright-field as bright dots (i.e., the pole of the rod-shaped bacteria) with a clear contrast against the background, squirming around in Brownian motion. The bright-field images were threshold processed and rendered with pseudo red color to visualize the bacteria (Figure 6e) and used instead in the bacteria count for *B. uniformis* at 24 h in coculture.

**Cell Line Authentication:** i) The mammalian cell lines (Caco-2, MDA-MB-231, HUVEC, and THP-1) were authenticated using short tandem repeat (STR) analysis. The STR analysis was performed with a cell pellet of about 2 million cells spun down with the media removed. The results were compared to an online database (e.g., Lonza, ATCC) to confirm the identity of a cell line. ii) Sanger sequencing (Functional Biosciences, funding NIH) of 16s rRNA gene from colony picks of a single morphology quadrant streak was used to confirm identity of the bacteria (*B. uniformis*) in the coculture experiment. 27 Forward (2\_27F universal 16s rRNA gene forward primer) and 1492 Reverse (2\_1492R universal 16s rRNA gene reverse primer) were used. Blast returned *B. uniformis* as top match in both cases, with 99.58% and 100% identity.

**Statistical Analysis:** Raw data were directly used in statistical analysis with no data excluded. Data were present as mean  $\pm$  s.d. The sample sizes (*n*) and *p* values were specified in the figure captions. All statistical analyses were performed using GraphPad Prism 9.2.0.

## Supporting Information

Supporting Information is available from the Wiley Online Library or from the author.

## Acknowledgements

This work was supported by NSF EFRI-1136903-EFRI-MKS, NIH R01 CA247479, NIH R01 A1154940, NIH R01 EB010039, NIH R01 CA185251, NIH R01 CA186134, NIH R01 CA181648, NIH P30CA014520, EPA H-MAP 83573701, American Cancer Society IRG-15-213-51 (Beebe Lab), and NIH R35GM124774 (Venturelli Lab). The authors thank Dr. Christopher Hartleb at the University of Wisconsin (UW)-Steven Points for demonstrating the (FireStingO<sub>2</sub>) optical oxygen sensor system, Dr. Evie Carchman from the Department of Surgery and UWCCC Biobank at the UW-Madison for the supply of colon tissue, McClean Lab from the Department of Biomedical Engineering at the UW-Madison for the supply of *C. albicans* (CMM16) sample, Huttenlocher Lab from the Department of Medical Microbiology

and Immunology at the UW-Madison for the performance of blood draw. Small molecule relative quantitation by LC/MS/MS was done at the UW School of Pharmacy, Analytical Instrumentation Center (AIC) Mass Spectrometry Facility. The authors thank Molly C. Pellitteri Hahn and Cameron O. Scarlett in the AIC for their valuable contributions. The authors also thank the UW Translational Research Initiatives in Pathology laboratory (TRIP), supported by the UW Department of Pathology and Laboratory Medicine, UWCCC and the Office of The Director-NIH (S10OD023526) for use of its facilities and STR Analysis services to perform cell line authentication, and the UW Optical Imaging Core for the support on the 3D confocal imaging. At last, the authors thank Dr. Jose M. Ayuso (Beebe Lab) for the introduction and early discussion upon the hypoxia dye in cell culture, and Mr. Duane S. Juang (Beebe Lab) for the inspiring conversation on the oxygen carrier function of fluorinated oil.

## Conflict of Interest

D.J.B. holds equity in BellBrook Labs LLC, Tasso Inc., Stacks to the Future LLC, Lynx Biosciences LLC, Onexio Biosystems LLC, Turba LLC, Flambeau Diagnostics LLC, and Salus Discovery LLC. D.J.B. is a consultant for Abbott Laboratories.

## Author Contributions

C.L. conceived the AROM (i.e., autonomously regulated oxygen microenvironments) method and designed the research. C.L., G.M.W., and M.H. performed COMSOL Multiphysics simulation of oxygen diffusion in multi-liquid-phase microsystems. C.L. designed and performed the UPLC-MS media analysis and data visualization with assistance from M.H., M.C.P.H., and C.O.S. C.L. designed and performed the POC and IOC measurements and data analysis, visualization with assistance from M.H., J.L., Y.F., H.H., and J.S. C.L. designed and performed the pH analysis in UOMS cell culture. C.L., M.H., K.P., B.C., and J.F. performed the cell culture/coculture experiments with assistance from J.L., Y.F., H.H., and J.S. J.F. constructed the fluorescently tagged *B. uniformis* strain, and B.C. carried out the preculture of bacteria with R.L.C. vetting the initial bacterial culture. C.L., M.H., and K.P. performed cell viability, IFS, and qPCR characterizations. C.L., M.H., and B.C. prepared the cell line authentication. D.J.B., O.S.V., and C.L. supervised experimental design, data analysis, and data presentation. C.L., D.J.B., M.H., and O.S.V. wrote the manuscript and all authors revised it.

## Data Availability Statement

The data that support the findings of this study are available from the corresponding authors upon reasonable request.

## Keywords

homeostasis, microscale cell culture, oxygen microenvironment, hypoxia, supply-demand balance

Received: October 11, 2021  
Revised: November 20, 2021  
Published online: February 4, 2022

- [1] A. Carreau, B. El Hafny-Rahbi, A. Matejuk, C. Grillon, C. Kieda, *J. Cell. Mol. Med.* **2011**, *15*, 1239.
- [2] L. Srikanth, M. M. Sunitha, K. Venkatesh, P. S. Kumar, C. Chandrasekhar, B. Vengamma, P. V. G. K. Sarma, *J. Stem Cells* **2015**, *10*, 97.

- [3] C. J. Drake, *Birth Defects Res. C: Embryo Today* **2003**, *69*, 73.
- [4] M. Z. Noman, M. Hasmmim, Y. Messai, S. Terry, C. Kieda, B. Janji, S. Chouaib, *Am. J. Physiol. Cell Physiol.* **2015**, *309*, C569.
- [5] C. T. Taylor, G. Doherty, P. G. Fallon, E. P. Cummins, *J. Clin. Invest.* **2016**, *126*, 3716.
- [6] V. Petrova, M. Annicchiarico-Petruzzelli, G. Melino, I. Amelio, *Oncogenesis* **2018**, *7*, 10.
- [7] N. E. Zeitouni, S. Chotikatam, M. von Köckritz-Blickwede, H. Y. Naim, *Mol. Cell. Pediatr.* **2016**, *3*, 14.
- [8] C. Michiels, C. Tellier, O. Feron, *Biochim. Biophys. Acta* **2016**, *1866*, 76.
- [9] H. K. Eltzschig, P. Carmeliet, *N. Engl. J. Med.* **2011**, *364*, 656.
- [10] M. G. V. Heiden, M. G. Vander Heiden, L. C. Cantley, C. B. Thompson, *Science* **2009**, *324*, 1029.
- [11] K. Flück, J. Fandrey, *Pflügers Arch.* **2016**, *468*, 77.
- [12] E. Krzywinska, C. Stockmann, *Biomedicines* **2018**, *6*, 56.
- [13] M. Mehling, S. Tay, *Curr. Opin. Biotechnol.* **2014**, *25*, 95.
- [14] G. M. Walker, H. C. Zeringue, D. J. Beebe, *Lab Chip* **2004**, *4*, 91.
- [15] E. W. K. Young, D. J. Beebe, *Chem. Soc. Rev.* **2010**, *39*, 1036.
- [16] S. N. Bhatia, D. E. Ingber, *Nat. Biotechnol.* **2014**, *32*, 760.
- [17] M. D. Brennan, M. L. Rexius-Hall, L. J. Elgass, D. T. Eddington, *Lab Chip* **2014**, *14*, 4305.
- [18] E. Berthier, E. W. K. Young, D. Beebe, *Lab Chip* **2012**, *12*, 1224.
- [19] H. E. Abaci, R. Devendra, Q. Smith, S. Gerech, G. Drazer, *Biomed. Microdevices* **2012**, *14*, 145.
- [20] E. Sinkala, D. T. Eddington, *Lab Chip* **2010**, *10*, 3291.
- [21] C. Li, M. Boban, A. Tuteja, *Lab Chip* **2017**, *17*, 1436.
- [22] E. J. Walsh, A. Feuerborn, J. H. R. Wheeler, A. N. Tan, W. M. Durham, K. R. Foster, P. R. Cook, *Nat. Commun.* **2017**, *8*, 816.
- [23] C. Li, J. Yu, J. Schehr, S. M. Berry, T. A. Leal, J. M. Lang, D. J. Beebe, *ACS Appl. Mater. Interfaces* **2018**, *10*, 17065.
- [24] C. Soitu, A. Feuerborn, A. N. Tan, H. Walker, P. A. Walsh, A. A. Castrejón-Pita, P. R. Cook, E. J. Walsh, *Proc. Natl. Acad. Sci. USA* **2018**, *115*, E5926.
- [25] C. Li, J. Yu, P. Paine, D. S. Juang, S. M. Berry, D. J. Beebe, *Lab Chip* **2018**, *18*, 2710.
- [26] W. Feng, Y. Chai, J. Forth, P. D. Ashby, T. P. Russell, B. A. Helms, *Nat. Commun.* **2019**, *10*, 1095.
- [27] C. Soitu, A. Feuerborn, C. Deroy, A. A. Castrejón-Pita, P. R. Cook, E. J. Walsh, *Sci. Adv.* **2019**, *5*, eaav8002.
- [28] C. Li, D. J. Niles, D. S. Juang, J. M. Lang, D. J. Beebe, *SLAS Technol.* **2019**, *24*, 535.
- [29] R. Battino, T. R. Rettich, T. Tominaga, *J. Phys. Chem. Ref. Data* **1983**, *12*, 163.
- [30] W. Xing, M. Yin, Q. Lv, Y. Hu, C. Liu, J. Zhang, *Rotating Electrode Methods and Oxygen Reduction Electrocatalysts*, Elsevier, Amsterdam **2014**, pp. 1–31.
- [31] T. L. Place, F. E. Domann, A. J. Case, *Free Radic. Biol. Med.* **2017**, *113*, 311.
- [32] K. Sklodowska, S. Jakiela, *RSC Adv.* **2017**, *7*, 40990.
- [33] C. Ding, F. A. N. Yurun, *Chin. J. Chem. Eng.* **2011**, *19*, 205.
- [34] W. L. Robb, *Ann. N. Y. Acad. Sci.* **1968**, *146*, 119.
- [35] L. Poulsen, P. R. Ogilby, *J. Phys. Chem. A* **2000**, *104*, 2573.
- [36] M. B. Byrne, M. T. Leslie, H. R. Gaskins, P. J. A. Kenis, *Trends Biotechnol.* **2014**, *32*, 556.
- [37] A. Prastowo, A. Feuerborn, P. R. Cook, E. J. Walsh, *Biomed. Microdevices* **2016**, *18*, 114.
- [38] C. Li, Z. Hite, J. W. Warrick, J. Li, S. H. Geller, V. G. Trantow, M. N. McClean, D. J. Beebe, *Sci. Adv.* **2020**, *6*, eaay9919.
- [39] A. B. Theberge, F. Courtois, Y. Schaerli, M. Fischlechner, C. Abell, F. Hoffelder, W. T. S. Huck, *Angew. Chem. Int. Ed.* **2010**, *49*, 5846.
- [40] F. Courtois, L. F. Olguin, G. Whyte, A. B. Theberge, W. T. S. Huck, F. Hoffelder, C. Abell, *Anal. Chem.* **2009**, *81*, 3008.
- [41] M. Decler, J. Jovanovic, A. Vakula, B. Udovicki, R.-S. Agoua, A. Madler, S. De Saeger, A. Rajkovic, *Toxins* **2018**, *10*, 266.

- [42] A. Reda, A. Refaat, A. A. Abd-Rabou, A. M. Mahmoud, M. Adel, S. Sabet, S. S. Ali, *Sci. Rep.* **2019**, *9*, 13748.
- [43] C. I. Jones 3rd, Z. Han, T. Presley, S. Varadharaj, J. L. Zweier, G. Ilan-govan, B. R. Alevriadou, *Am. J. Physiol. Cell Physiol.* **2008**, *295*, C180.
- [44] M. Reiss, D. Roos, *J. Clin. Invest.* **1978**, *61*, 480.
- [45] J. M. Lambooi, M. A. Hoogenkamp, B. W. Brandt, M. M. Janus, B. P. Krom, *Fungal Genet. Biol.* **2017**, *109*, 1.
- [46] L. Goers, P. Freemont, K. M. Polizzi, *J. R. Soc. Interface* **2014**, *11*, 20140065.
- [47] P. Shah, J. V. Fritz, E. Glaab, M. S. Desai, K. Greenhalgh, A. Frachet, M. Niegowska, M. Estes, C. Jäger, C. Seguin-Devaux, F. Zenhausern, P. Wilmes, *Nat. Commun.* **2016**, *7*, 11535.
- [48] A. Bein, W. Shin, S. Jalili-Firoozinezhad, M. H. Park, A. Sontheimer-Phelps, A. Tovaglieri, A. Chalkiadaki, H. J. Kim, D. E. Ingber, *Cell. Mol. Gastroenterol. Hepatol.* **2018**, *5*, 659.
- [49] C. Michiels, *Am. J. Pathol.* **2004**, *164*, 1875.
- [50] H. Sun, E. C. Chow, S. Liu, Y. Du, K. S. Pang, *Expert Opin. Drug Metab. Toxicol.* **2008**, *4*, 395.
- [51] J. M. Allaire, S. M. Crowley, H. T. Law, S.-Y. Chang, H.-J. Ko, B. A. Vallance, *Trends Immunol.* **2019**, *40*, 174.
- [52] J. A. Imlay, *Adv. Microb. Physiol.* **2002**, *46*, 111.
- [53] H. M. Wexler, *Clin. Microbiol. Rev.* **2007**, *20*, 593.
- [54] A. D. Baughn, M. H. Malamy, *Nature* **2004**, *427*, 441.
- [55] H. Liu, M. N. Price, H. K. Carlson, Y. Chen, J. Ray, A. L. Shiver, C. J. Petzold, K. C. Huang, A. P. Arkin, A. M. Deutschbauer, *bioRxiv*:10.1101/573055, **2019**. <https://www.biorxiv.org/content/10.1101/573055v1.full>.
- [56] C. J. Sund, E. R. Rocha, A. O. Tzianabos, W. G. Wells, J. M. Gee, M. A. Reott, D. P. O'Rourke, C. J. Smith, *Mol. Microbiol.* **2008**, *67*, 129.
- [57] L. Rigottier-Gois, *ISME J.* **2013**, *7*, 1256.
- [58] B. A. Wagner, S. Venkataraman, G. R. Buettner, *Free Radic. Biol. Med.* **2011**, *51*, 700.
- [59] M.-C. Kim, R. H. W. Lam, T. Thorsen, H. H. Asada, *Microfluid. Nanofluid.* **2013**, *15*, 285.
- [60] S. R. McKeown, *Br. J. Radiol.* **2014**, *87*, 20130676.
- [61] M. M. Mahe, N. Sundaram, C. L. Watson, N. F. Shroyer, M. A. Helmrath, *J. Vis. Exp.* **2015**, *97*, 52483.
- [62] K. L. VanDussen, J. M. Marinshaw, N. Shaikh, H. Miyoshi, C. Moon, P. I. Tarr, M. A. Ciorba, T. S. Stappenbeck, *Gut* **2015**, *64*, 911.
- [63] W. R. Whitaker, E. S. Shepherd, J. L. Sonnenburg, *Cell* **2017**, *169*, 538.
- [64] N. M. Koropatkin, E. C. Martens, J. I. Gordon, T. J. Smith, *Structure* **2008**, *16*, 1105.
- [65] J. Larsbrink, T. E. Rogers, G. R. Hemsworth, L. S. McKee, A. S. Tazuin, O. Spadiut, S. Klintner, N. A. Pudlo, K. Urs, N. M. Koropatkin, A. L. Creagh, C. A. Haynes, A. G. Kelly, S. N. Cederholm, G. J. Davies, E. C. Martens, H. Brumer, *Nature* **2014**, *506*, 498.
- [66] E. C. Martens, H. C. Chiang, J. I. Gordon, *Cell Host Microbe* **2008**, *4*, 447.
- [67] J. Wang, N. B. Shoemaker, G. R. Wang, A. A. Salyers, *J. Bacteriol.* **2000**, *182*, 3559.